SpIES: THE *SPITZER* IRAC EQUATORIAL SURVEY

John D. Timlin[1,*], Nicholas P. Ross[1,2], Gordon T. Richards[1], Mark Lacy[3], Erin L. Ryan[4], Robert B. Stone[1], Franz E. Bauer[5,6,7], W. N. Brandt[8,9,10], Xiaohui Fan[11], Eilat Glikman[12], Daryl Haggard[13], Linhua Jiang[14], Stephanie M. LaMassa[15], Yen-Ting Lin[16], Martin Makler[17], Peregrine McGehee[18], Adam D. Myers[19], Donald P. Schneider[8,9], C. Megan Urry[15], Edward J. Wollack[20], Nadia L. Zakamska[21]

(Dated: December 29, 2015)
Draft version December 29, 2015

ABSTRACT

We describe the first data release from the *Spitzer*-IRAC Equatorial Survey (SpIES); a large-area survey of ∼115 deg^2 in the Equatorial SDSS Stripe 82 field using *Spitzer* during its 'warm' mission phase. SpIES was designed to probe sufficient volume to perform measurements of quasar clustering and the luminosity function at $z \geq 3$ to test various models for "feedback" from active galactic nuclei (AGN). Additionally, the wide range of available multi-wavelength, multi-epoch ancillary data enables SpIES to identify both high-redshift ($z \geq 5$) quasars as well as obscured quasars missed by optical surveys. SpIES achieves 5σ depths of 6.13 μJy (21.93 AB magnitude) and 5.75 μJy (22.0 AB magnitude) at 3.6 and 4.5 microns, respectively—depths significantly fainter than the *WISE* AllSky survey. We show that the SpIES survey recovers a much larger fraction of spectroscopically-confirmed quasars (∼98%) in Stripe 82 than are recovered by *WISE* (∼55%). This depth is especially powerful at high-redshift ($z \geq 3.5$), where SpIES recovers 94% of confirmed quasars, whereas *WISE* only recovers 25%. Here we define the SpIES survey parameters and describe the image processing, source extraction, and catalog production methods used to analyze the SpIES data. In addition to this survey paper, we release 234 images created by the SpIES team and three detection catalogs: a 3.6 μm-only detection catalog containing ∼6.1 million sources, a 4.5 μm-only detection catalog containing ∼6.5 million sources, and a dual-band detection catalog containing ∼5.4 million sources.

Subject headings: surveys - quasars: Mid-Infrared; *Spitzer*

* For correspondence regarding this article, please write to J. D. Timlin: john.d.timlin@drexel.edu

[1] Department of Physics, Drexel University, 3141 Chestnut Street, Philadelphia, PA 19104, U.S.A

[2] Institute for Astronomy, University of Edinburgh, Royal Observatory, Edinburgh, EH9 3HJ, U.K.

[3] National Radio Astronomy Observatory, 520 Edgemont Road, Charlottesville, VA 22903, U.S.A

[4] University of Maryland Department of Astronomy, College Park, MD 20742, U.S.A

[5] Instituto de Astrofísica, Facultad de Física, Pontificia Universidad Católica de Chile, Casilla 306, Santiago 22, Chile

[6] Millennium Institute of Astrophysics, MAS, Nuncio Monseñor Sótero Sanz 100, Providencia, Santiago de Chile

[7] Space Science Institute, 4750 Walnut Street, Suite 205, Boulder, Colorado 80301

[8] Department of Astronomy & Astrophysics, 525 Davey Lab, The Pennsylvania State University, University Park, PA 16802, USA

[9] Institute for Gravitation and the Cosmos, The Pennsylvania State University, University Park, PA 16802, USA

[10] Department of Physics, 104 Davey Lab, The Pennsylvania State University, University Park, PA 16802, USA

[11] Steward Observatory, University of Arizona, Tucson, AZ 85721, USA

[12] Department of Physics, Middlebury College, Middlebury, VT 05753, USA

[13] Department of Physics and Astronomy, Amherst College, Amherst, MA 01002-5000, USA

[14] Kavli Institute for Astronomy and Astrophysics, Peking University, Beijing 100871, China

[15] Yale Center for Astronomy and Astrophysics, Yale University, Physics Department, PO Box 208120, New Haven, CT, 06520-8120, USA

[16] Institute of Astronomy and Astrophysics, Academia Sinica, Taipei 106, Taiwan

[17] Centro Brasileiro de Pesquisas Físicas

[18] IPAC, 1200 E. California Blvd, Pasadena, CA 91125

[19] Department of Physics and Astronomy, University of Wyoming, 1000 University Ave., Laramie, WY, 82071, USA

[20] NASA Goddard Space Flight Center, Greenbelt, MD 20771

[21] Department of Physics and Astronomy, Johns Hopkins University, Bloomberg Center, 3400 N. Charles St., Baltimore, MD 21218, USA

1. INTRODUCTION

The *Spitzer* Space Telescope (Werner et al. 2004) has been paramount in understanding the Universe at mid-infrared wavelengths. During its primary mission, *Spitzer* observed at 3.6, 4.5, 5.8, and 8.0 μm using the Infrared Array Camera (IRAC; Fazio et al. 2004), at 24, 70, and 160 μm using the Multiband Imaging Photometer for *Spitzer* (MIPS; Rieke et al. 2004) camera, and had a dedicated infrared spectrograph (IRS; Houck et al. 2004) covering wavelengths from 5.3 to 38 μm. Since the exhaustion of its cryogen in 2009, *Spitzer* has run its 'warm' mission phase, taking images with the two shortest IRAC passbands (3.6 and 4.5 μm).

Spitzer IRAC has been a valuable tool in the creation of deep, relatively small area surveys through campaigns like the $\sim$2 deg^2 Spitzer-COSMOS survey (S-COSMOS; Sanders et al. 2007) and the $\sim$10 deg^2 *Spitzer* Deep, Wide-field Survey (SDWFS; Ashby et al. 2009) utilizing all four of the IRAC bands. *Spitzer* continues to delve deeper in its 'warm' phase with the IRAC ultradeep filed (IUDF; Labbe et al. 2015), the $\sim$1.2 deg^2 *Spitzer* Large Area Survey with Hyper-Suprime-Cam (SPLASH; Steinhardt et al. 2014), and the $\sim$18 deg^2 *Spitzer* Extragalactic Representative Volume Survey (SERVS; Mauduit et al. 2012).

Despite having a relatively small $5.'2\times5.'2$ field of view (FOV), IRAC has also effectively and efficiently run larger-area programs throughout its lifetime such as the $\sim$65 deg^2 SIRTF Wide-Area Infrared Extragalactic Survey (SWIRE; Lonsdale et al. 2003). Recently, *Spitzer* has made an effort to run larger-area surveys in the 'warm' phase with the $\sim$26 deg^2 *Spitzer*-HETDEX Exploratory Large Area (SHELA; Papovich et al. 2011) and the $\sim$94 deg^2 *Spitzer* South Pole Telescope Deep Field (SSDF; Ashby et al. 2013) mission which, until now, had the largest area of any *Spitzer* survey.

These large-area campaigns are made possible by the IRAC mapping mode strategy, which aligns the arrays on a positional grid, allowing observations to overlap through successive motions in the grid. This approach differs from other observing strategies, many of which forced the telescope to slew to a single position multiple times to observe the same location on the sky in a different channel (see Section 3.2 of the IRAC Instrument Handbook[23]). Mapping mode decreases slew time, allowing for larger area surveys to be performed while still reaching interesting flux limits.

Spitzer is not the only telescope performing large area, mid-infrared observations of the Universe. The Wide-field Infrared Survey Explorer (*WISE*; Wright et al. 2010) telescope has been mapping the entire sky in four channels, two of which have nearly the same wavelength as 'warm' *Spitzer* (3.4 and 4.6 μm). While *WISE* covers essentially the entire sky, it lacks both the depth and the spatial resolution that *Spitzer* IRAC surveys can achieve.

The combined depth and area of the *Spitzer* IRAC Equatorial Survey (SpIES), along with the wealth of multi-wavelength, multi-epoch ancillary imaging and spectroscopic data on Stripe 82 (S82; Stoughton et al. 2002; Annis et al. 2014; Jiang et al. 2014), make it a

---

TABLE 1
THE *Spitzer* IRAC EQUATORIAL SURVEY (SpIES) KEY PARAMETERS

Parameter	Value
Imaging	IRAC Ch1 and Ch2
Wavelength	3.6 and 4.5 μm
Area[a]	$\sim$115 deg^2
No. of IRAC pointings	$\sim$70,000
Exposure Time at each pointing	60s
Total Observation Time	820hr
Typical Zodiacal Background	$0.09 - 0.23$ MJy sr^{-1}
IRAC PSF FWHM[b]	$1.''95, 2.''02$
Total number of objects[c]	$\sim$5,400,000
Limiting AB Magnitude[d] (5σ)	21.93, 22.0
Data URL:	
http://www.physics.drexel.edu/~gtr/spies/	

NOTE. — [a] Total survey area covered by both detectors. The area covered by a single detector decreases due to their separation on IRAC (details in Section 3). [b]5σ dual-band detection catalog (see Section 5). [c]Total number of objects in the dual-band catalog. [d]Values are for the 3.6 μm, 4.5 μm detectors.

---

powerful tool for addressing a wide range of topics in contemporary astrophysics. In particular, we seek to use the data to: probe the population of obscured quasars at high redshift (e.g., Alexandroff et al. 2013; Glikman et al. 2013; Assef et al. 2015); use high-redshift unobscured quasars to investigate how quasar feedback contributes to galaxy evolution (e.g., Hopkins et al. 2007; White et al. 2012); improve the removal of foreground objects from maps of the cosmic microwave background (Wang et al. 2006); better constrain the stellar masses of Lyman Break Galaxies (e.g., Daddi et al. 2007; improve stellar population modeling for hosts of supernovae (e.g., Sullivan et al. 2010; Fox et al. 2015); and enable discovery of cool stars (e.g., Lucas et al. 2010).

In this paper, we describe the SpIES survey parameters and catalogs. SpIES mapped a large portion of the Sloan Digital Sky Survey (SDSS; York et al. 2000) equatorial S82 field (Stoughton et al. 2002; Annis et al. 2014; Jiang et al. 2014), utilizing the *Spitzer* 3.6 and 4.5 μm bands (often referred to as Ch1 and Ch2 respectively). Collecting $\sim$115 deg^2 over $\sim$820 hours, SpIES is the largest area *Spitzer* survey, probing to depths comparable to SWIRE. Table 1 contains the key parameters of SpIES such as the wavelengths and point spread function of IRAC, along with the observation times, area, and depth of the SpIES survey. With this release, we present three SpIES source catalogs consisting of $\sim$6.1 million objects detected only at 3.6 μm, $\sim$6.6 million objects detected only at 4.5 μm, and a dual-band detection catalog which contains $\sim$5.4 million detections in both bands. We also release the images generated by the SpIES team used to build the catalogs described herein.

We begin our discussion by describing the existing data covering the S82 footprint in Section 2, followed by the *Spitzer* observation strategy used for SpIES in Section 3. We discuss the data products from *Spitzer* and our image stacking process in Section 4. The SpIES catalogs are described Section 5, which includes source extraction techniques, photometric errors, and astrometric reliability. This section also discusses the completeness, number counts, and depth of the SpIES detection catalog.
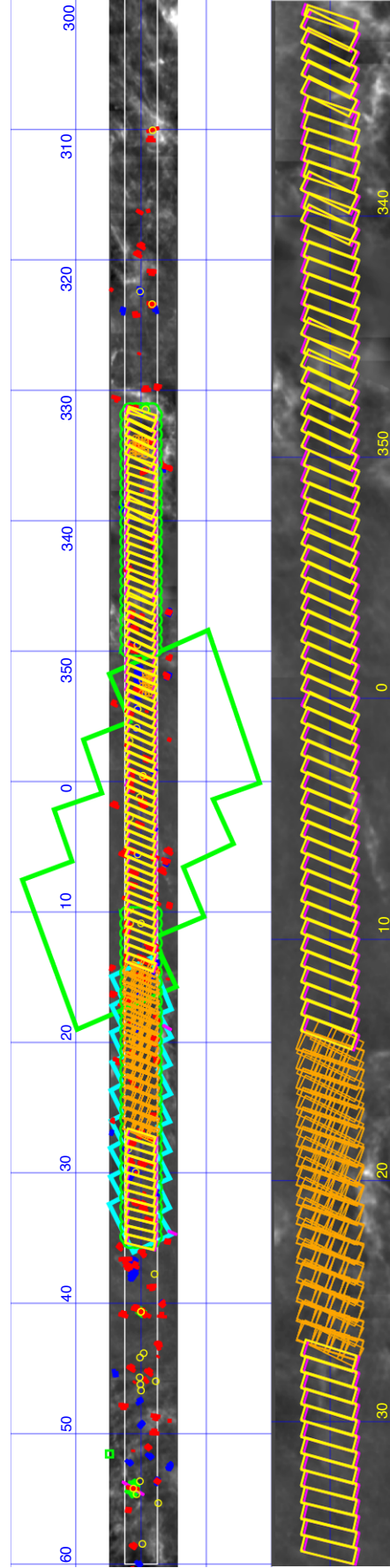
FIG. 1.— Top: We show the SpIES coverage area (yellow and purple rectangles) atop the $100\mu m$ IRAS dust map (Schlegel et al. 1998) of the full SDSS Stripe 82 region (white box). Many different surveys have covered this region of the sky and overlap with SpIES. Displayed are the HeLMS (green box) and HeRS (light blue) survey footprints (Oliver et al. 2012; Viero et al. 2014), the regions observed by *XMM-Newton* (yellow and orange circles) and *Chandra* (red circles were observed with the ACIS-I arrays; LaMassa et al. 2013a,b), the VLA (green scallop) from Hodge et al. (2011), and the SHELA observations (orange boxes) by Papovich et al. (2011), as a few examples of many surveys that cover the S82 region. More details about other surveys on S82 can be found in Table 2. Bottom: Detailed SpIES Ch1 (yellow) and Ch2 (purple) coverage of Stripe 82 along with SHELA coverage (orange). Both panels are centered on $\delta=0$ and α values are given in J2000 degrees.

Finally, in Section 6, we match SpIES objects to various quasar catalogs to test the SpIES recovery fraction of high-redshift quasars. We also provide a summary of the SpIES survey and data products.

We calculate magnitudes on the AB scale, which has a flux density zeropoint of 3631 Jy (Oke & Gunn 1983). These are denoted as [3.6] and [4.5], respectively. Conversion to Vega magnitudes is given by [3.6]−2.779 and [4.5]−3.264, respectively (calculated using the Vega zeropoint flux density values of 280.9 Jy at 3.6 μm and 179.7 Jy at 4.5 μm from Table 4.1 in the IRAC Handbook[23]).

2. THE STRIPE 82 REGION

The observational goal of the SpIES project was to map S82 in order to provide a suitably large "laboratory" in which to conduct the types of experiments that involve rare objects, as noted above. S82 is located on the Celestial Equator spanning a range of $-60° \leq \alpha \leq 60°$ and $-1.25° \leq \delta \leq 1.25°$. The SpIES observations cover approximately one third of this region centered on $\delta = 0°$ and spanning the range from $-30° \leq \alpha \leq 35°$, with a break in coverage between $13.9° \leq \alpha \leq 27.2°$ where deeper IRAC data exists from the SHELA (Papovich et al. 2011) survey. Within those RA limits, SpIES completely covers S82 from $-0.85° \leq \delta \leq 0.85°$ with irregular coverage outside of that declination range due to the orientation of observations (see Figure 1). The SpIES footprint was chosen to take advantage of the SHELA footprint and for its relatively low background at mid-infrared wavelengths. As described in more detail in Section 5.5, background noise can drastically decrease the depth of the survey, which makes observing the faintest sources prohibitively difficult.

SDSS observed S82 in five optical filters (*ugriz*; Fukugita et al. 1996) to find variable objects and to obtain deeper imaging than the wider-area SDSS observations in the Northern Galactic Cap (York et al. 2000; Frieman et al. 2008; Annis et al. 2014). SDSS-I/II observed the full S82 field ∼80 times over 8 years resulting in photometry which reaches nearly two magnitudes fainter than the other fields in the survey (Annis et al. 2014, Jiang et al. 2014). S82 has also been observed multiple times with the SDSS spectrographs (Smee et al. 2013) as part of the SDSS-I/II (York et al. 2000) and SDSS-III/BOSS (Eisenstein et al. 2011) campaigns, along with spectra from other facilities such as 2dF, 6dF, and AUS (Croom et al. 2004, 2009), WiggleZ (Drinkwater et al. 2010), the Virmos-VLT Deep Survey (VVDS; Le Fèvre et al. 2005), the VIMOS Public Extragalactic Redshift Survey (VIPERS1; de la Torre et al. 2013), DEEP2 (Davis et al. 2007), and the Prism Multi-Object Survey (PRIMUS; Coil et al. 2011). In total these facilities have collected ∼125,000 high quality spectra across its entire area.

In addition to the collection of deep SDSS optical imaging (reaching a 5σ AB magnitude of 24.6 in the r-band) and spectra, S82 contains a vast amount of multi-wavelength imaging taken over many epochs. The two panels of Figure 1 show several multi-wavelength surveys that overlap with the SpIES region. At radio wavelengths, in addition to full coverage by the Faint Images of the Radio Sky at Twenty-centimeters (FIRST; Becker et al. 1995, Helfand et al. 2015) survey, Hodge et al. (2011) provided 1″8 resolution data down to 52μJy at

1.4GHz (L-band) over ∼90 deg^2 of Stripe 82 (twice the resolution and three times the depth of FIRST). Additional radio data will be forthcoming at lower resolution (e.g., Jarvis et al. 2014) and at higher frequency (Mooley et al. 2014).

In the far-infrared, the Herschel Space Observatory performed the HerMES Large Mode Survey (HeLMS; Oliver et al. 2012) and the Herschel Stripe 82 Survey (HerS; Viero et al. 2014) to study galaxy formation and correlations between galaxies and dark matter haloes. Existing mid-infrared observations of S82 include SHELA (Papovich et al. 2011), which contains deep imaging data for dark energy measurements, and the AllWISE observations from *WISE* (Wright et al. 2010). Near-infrared measurements of S82 have been performed by the UKIRT Infrared Deep Sky Survey (UKIDSS; Lawrence et al. 2007), the VISTA Hemisphere Survey (VHS; McMahon et al. 2013)—which is matched to the SDSS coadd photometry in the catalog presented in Bundy et al. (2015)—and the deeper J- and K-band coverage from the VISTA-CFHT Stripe 82 Survey over 130 deg^2 of S82 (VICS82, Geach et al. in prep.). In addition to SDSS, Stripe 82 has high-resolution imaging (median seeing of 0″6) from the CFHT Stripe 82 Survey (CS82, Kneib et al. in prep.) and is part of the Dark Energy Survey[24] (DES) footprint.

S82 was also mapped in the ultraviolet as part of the *GALEX* All-sky Imaging Survey and Medium Imaging Survey, and a few locations were imaged with the Deep Imaging Survey as outlined in Martin et al. (2005). *Chandra* and *XMM-Newton* have been used to observe partly contiguous regions over a wide area at X-ray wavelengths, searching for high luminosity quasars (LaMassa et al. 2013a,b), with the most recent large-area X-ray catalog release covering ∼31deg^2 with *XMM-Newton* (LaMassa et al. 2015). More observations are cited in Table 2 which lists some properties of the deepest imaging data of S82 at various wavelengths. The combination of all of the multi-epoch, multi-wavelength spectroscopic and photometric data on S82 provides a powerful tool to aid in our understanding of the Universe by painting a multi-wavelength and multi-epoch picture of matched objects between these surveys.

3. DATA ACQUISITION

SpIES data were obtained as part of Cycle 9 (2012-2014) of the *Spitzer* 'warm' post-cryogenic mission utilizing the first two channels of IRAC. IRAC is a wide-field camera with four channels, each 256×256 pixels with a 5′2×5′2 field of view (Fazio et al. 2004). The first two arrays (3.6 and 4.5 microns) are designed to observe the sky simultaneously, which decreases observation time and ensures that the epochs of measurement are roughly the same for both channels. *Spitzer* has been operating in 'warm' mode long enough to measure and report the differences in IRAC performance between the cryogenic and 'warm' observations[25]. The changes in performance, including changes in PSF, sensitivity levels, and constant values such as gain and flux conversion, are minor and

---

[24]http://www.darkenergysurvey.org/
[25]http://irsa.ipac.caltech.edu/data/SPITZER/ docs/irac/warmimgcharacteristics/

TABLE 2
Deep imaging data available on Stripe 82

Waveband λ_{eff} (μm)	Origin	Depth	Coverage (deg^2)	Reference
2-10 keV	XMM-*Newton*	$4.7\times^{-15}$ erg s^{-1} cm^{-2}	31.3[a]	LaMassa et al. (2015)
0.5-2 keV	XMM-*Newton*	$8.7\times^{-16}$ erg s^{-1} cm^{-2}	31.3[a]	LaMassa et al. (2015)
FUV, 1350–1750 Å	GALEX	$m_{AB} \simeq 23$	∼200	Martin et al. (2005)
NUV, 1750–2750 Å	GALEX	$m_{AB} \simeq 23$	∼200	Martin et al. (2005)
0.355 (u)	SDSS	$m_{AB} = 23.90$	∼300	Jiang et al. (2014)
0.5 (g)	SDSS	$m_{AB} = 25.10$	∼300	Jiang et al. (2014)
	HSC[b]	$m_{AB} = 26.50$	∼300	Miyazaki et al.
	DES	$m_{AB} = 26.50$	∼300	Diehl et al. (2014)
0.6 (r)	SDSS	$m_{AB} = 24, 60$	∼300	Jiang et al. (2014)
	HSC[b]	$m_{AB} = 26.10$	∼300	Miyazaki et al.
	DES	$m_{AB} = 26.00$	∼300	Diehl et al. (2014)
0.7 (i)	SDSS	$m_{AB} = 24.10$	∼300	Jiang et al. (2014)
	HSC[b]	$m_{AB} = 25.90$	∼300	Miyazaki et al.
	CS82	$m_{AB} = 24.00$	∼170	Kneib et al. in prep.
	DES	$m_{AB} = 25.30$	∼300	Diehl et al. (2014)
0.9 (z)	SDSS	$m_{AB} = 22.80$	∼300	Jiang et al. (2014)
	HSC[b]	$m_{AB} = 25.10$	∼300	Miyazaki et al.
	DES	$m_{AB} = 24.70$	∼300	Diehl et al. (2014)
1.00 (Y)	ULAS[c]	$m_{AB} = 20.93$	277.5	Lawrence et al. (2007)
	HSC[b]	$m_{AB} = 24.40$	∼300	Miyazaki et al.
	DES	$m_{AB} = 23.00$	∼300	Diehl et al. (2014)
	VHS	$m_{AB} = 21.20$	∼300	McMahon et al. (2013)
1.35 (J)	ULAS[c]	$m_{AB} = 20.44, 24\,\mu$Jy	277.5	Lawrence et al. (2007)
	VICS82,	$m_{AB} = 22.70$	150	Geach et al. in prep.
	VHS	$m_{AB} = 22.20$	∼300	McMahon et al. (2013)
1.65 (H)	ULAS[c]	$m_{AB} = 19.98, 37\,\mu$Jy	277.5	Lawrence et al. (2007)
	VHS	$m_{AB} = 20.60$	∼300	McMahon et al. (2013)
2.20 (K_s)	ULAS[c]	$m_{AB} = 20.10, 33\,\mu$Jy	277.5	Lawrence et al. (2007)
	VICS82	$m_{AB} = 21.60$	150	Geach et al. in prep.
	VHS	$m_{AB} = 21.50$	∼300	McMahon et al. (2013)
3.6 (Ch1)	**SpIES**	$m_{AB} = 21.90$	∼115	**this paper**
	SHELA	$m_{AB} = 22.05$	∼26	Papovich et al. (2011)
4.5 (Ch2)	**SpIES**	$m_{AB} = 22.00$	∼115	**this paper**
	SHELA	$m_{AB} = 22.05$	∼26	Papovich et al. (2011)
250	*Hershel*/SPIRE	64.0, 64.0 mJy	270, 79	Oliver et al. (2012); Viero et al. (2014)
350	*Hershel*/SPIRE	64.5, 64.5 mJy	270, 79	Oliver et al. (2012); Viero et al. (2014)
500	*Hershel*/SPIRE	74.0, 74.0 mJy	270, 79	Oliver et al. (2012); Viero et al. (2014)
1100 (277 GHz)	ACT[d]	∼6.4 mJy	300	analysis under way
1400 (218 GHz)	ACT[d]	∼3.3 mJy	300	Gralla et al. (2014); Das et al. (2014)
2000 (148 GHz)	ACT[d]	∼2.2 mJy	300	Gralla et al. (2014); Das et al. (2014)
21,000 (L-band)	VLA[e]	260 μJy	92	Hodge et al. (2011)
30,000 (S-band)	VLA[e]	400 μJy	∼300	Mooley et al. (2014)

NOTE. — [a]Includes 7.4 deg^2 of archival *Chandra* data, [b]Hyper Suprime-Cam (see http://www.naoj.org/Projects/HSC/surveyplan.html for more details), [c]UKIDSS Large Area Survey, [d]Atacama Cosmology Telescope, [e]Very Large Array

the overall performance of IRAC has not degraded substantially with time (see Mauduit et al. 2012).

The SpIES observation strategy was motivated by the strategies of previous *Spitzer* campaigns such as SDWFS (Ashby et al. 2009), SWIRE (Lonsdale et al. 2003), SERVS (Mauduit et al. 2012), and SSDF (Ashby et al. 2013). Similar to these surveys, SpIES observations were separated into individual Astronomical Observation Requests (AORs), which are self-contained exposure sequences executed independently of each other. AORs are comprised of sequential pointings of IRAC which are stacked to form a single image. AORs overlap slightly, to form the entire field (see the SpIES regions in Figure 1). Most of the SpIES AORs consist of a map of 8×28 IRAC

FOVs, corresponding to a total area of ∼1.63 deg^2 per AOR (see Figure 2). There were, however, a few AORs which needed to be adjusted in width due to changes in position angle between AOR observations (observations separated by ∼6 months have a field rotation of ∼180°), to connect with their neighboring AORs and form a continuous strip. Four of our AORs were increased to 9×28 pointings, two were increased to 10×28 pointings, and one was decreased to 5×28 pointings. The size differences can be identified by an increase or decrease of the given AOR integration time in Appendix A. In total, SpIES is comprised of 154 AORs observed over two epochs (77 AORs per epoch) which corresponds to ∼70,000 IRAC fields of view spanning the full survey area.

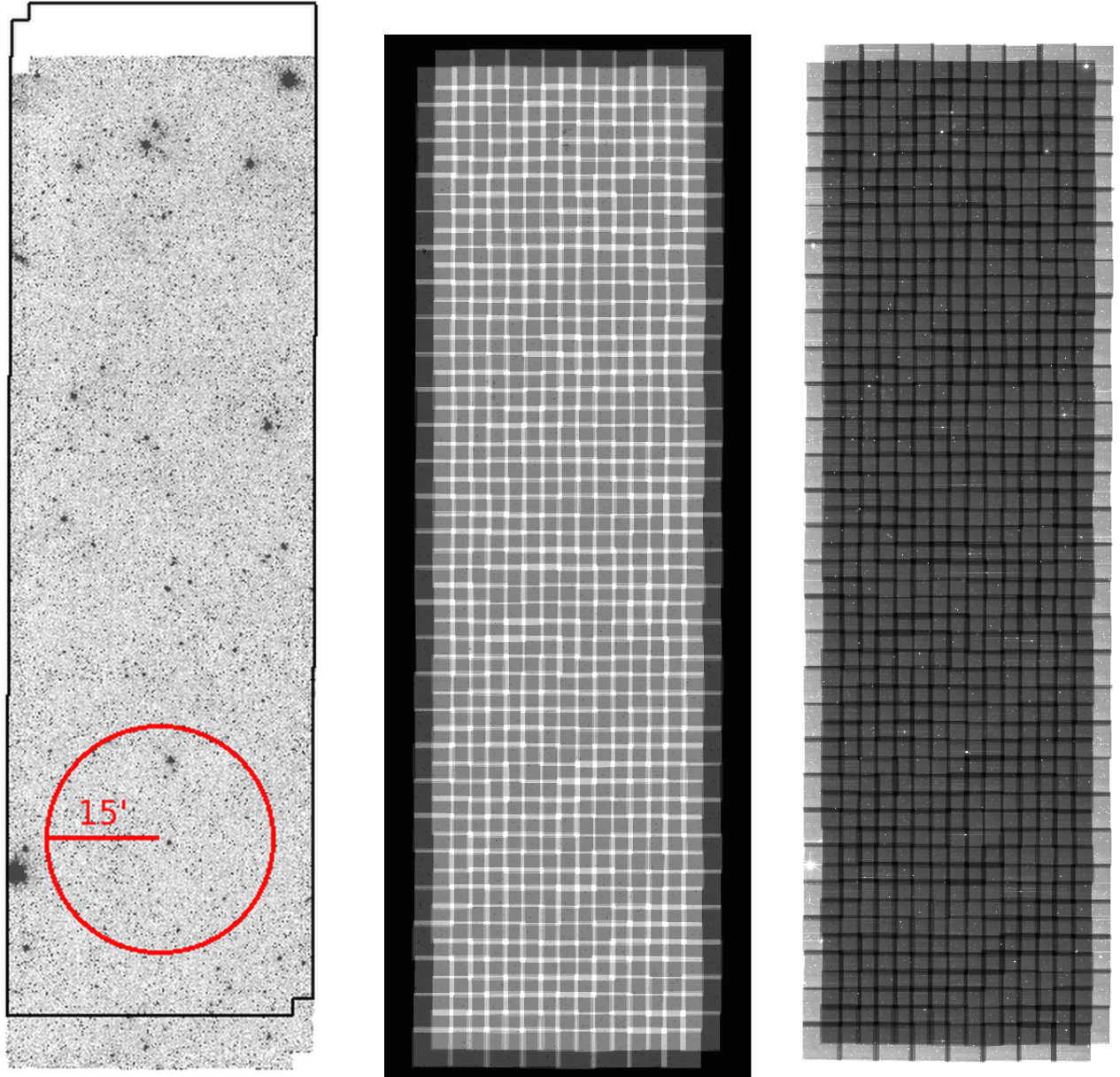FIG. 2.— Left: One SpIES $3.6\,\mu$m, double-epoch, stacked AOR from which we extract sources. This is one of 77 stacked AORs (154 single epoch AORs divided by two epochs) that are strung together (see Figure 1) to cover the entire SpIES field. The red circular region illustrates the angular size of the Moon, and the black region shows the coverage of the same AOR at $4.5\,\mu$m. Center: An example of the coverage map of the AOR, showing where the individual pointings of IRAC overlap when they are combined to form the AOR. These maps are unique to each AOR and are used as weighted images during source extraction. Pixels with lighter colors have a more coverages. The AOR footprint has been padded with a band corresponding to zero coverage. Right: The flux density uncertainty map of each AOR, where the values only take into account details in pipeline processing error propagation, not source extraction. In this map, darker colors, correspond to lower uncertainties in flux density. The lower uncertainties align with the higher coverage values shown in the central panel.

Each AOR was built by successively pointing and dithering IRAC until the 8×28 map was complete, using a small-cycle dither pattern. This pattern offsets the observations by up to 11 pixels ($\sim13''$) to obtain overlapping coverage while eliminating some instrumental problems such as bad pixel detections and bright star saturation (Mauduit et al. 2012). Built into the cycle dither pattern is a sub-pixel dither pattern of half a pixel, which improves the $1''\!.2$ per pixel sampling to $0''\!.6$ per pixel after the images are stacked. This oversampling reduces

effects that bad pixels and bright star saturation have on the image. This issue must be accounted for when calculating source flux error in Section 5.

Images are taken simultaneously at $3.6\,\mu$m and $4.5\,\mu$m with a $\sim6'\!.7$ offset between the two channels due to the physical placement of the arrays. This offset leads to a section around the perimeter where objects are detected in one band and not the other due to the placement of the detectors (as shown in Figure 2). The catalogs described in Section 5.3 indicate which objects lack a counterpart

TABLE 3
ASTRONOMICAL OBSERVATION REQUEST (AOR)
TIME TABLE

Operation	Time (s)
Exposure time at each pointing	30
×2 dithering	60
× ~224 pointings	13440
+ Slew Time	~2400
+ Settle Time	~2400
+ Overhead(Slew and Download)	~600
×2 epochs	~37700
×77 AORs	~2.9×10^6
Total Observation Time	~820hr

NOTE. — Approximate exposure time breakdown for SpIES for each detector (the larger AORs required more time than estimated). The two dithering and the two epochs combined with 30s exposures each lead to a total AOR exposure time of $2×2×30 = 120$s for both channels. SpIES spent ~70% of the time in observation and ~30% in motion to other fields.

in the other band due to these regions without overlapping dual-band coverage. Additionally, the survey area changes slightly due to this offset. The quoted area of ~115 deg^2 is the coverage where SpIES detects sources at either 3.6 μm or 4.5 μm. The coverage of each individual detector is ~107 deg^2 where the coverage of the overlap of the two detectors (detections at both 3.6 μm and 4.5 μm) is ~100 deg^2. This will be important when computing number density in Section 5.5.
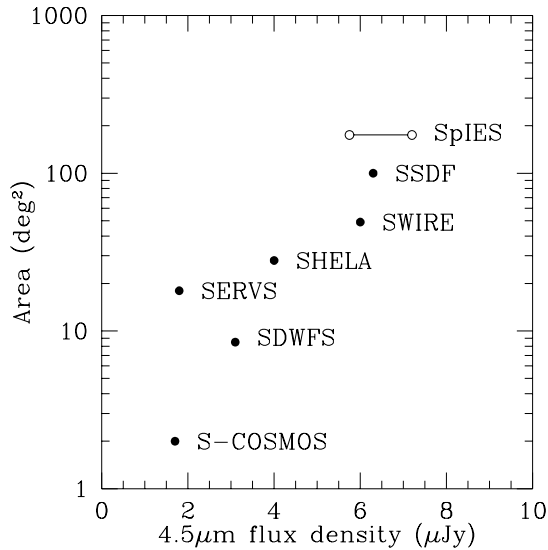

FIG. 3.— Comparison of the calculated 4.5 μm 5σ depth to area of the major *Spitzer* surveys. Depths are calculated using the *Spitzer* Sensitivity Performance Estimation Tool (SENS-PET) assuming a low background. At ~115 deg^2 in area SpIES is the largest *Spitzer* survey and probes SWIRE depths (Lonsdale et al. 2003). Open circles show the measured depth (left; see Table 9) and calculated depth from SENS-PET with a medium background (right) for SpIES.

Observations were performed over two distinct epochs separated by no less than five hours in time (see Appendix A) and shifted by half a FOV in both right ascension and declination. Multiple epoch observations allow for detection of transient objects, and the spatial offset

ensures that detected objects are observed on different regions of the array, allowing for more accurate photometry. In most cases, the second epoch of observation was taken directly after the first, where the observation time for the first epoch of a full AOR (~5 hours including slew and settle time) was sufficient to significantly separate the two epochs. For a typical asteroid, which moves at ~25″ hr^{-1} (Ashby et al. 2009), a five-hour temporal separation leads to ~2′ spatial separation, which is easily detected in separate epochs. The SpIES field is covered with at least four exposures at each pixel, providing both deep and reliable photometry across the large area of observation—with an exception around the perimeter where the second epoch has been shifted by half a field of view.

The SpIES AORs were constructed to maximize area while maintaining a depth comparable to that of SWIRE (Lonsdale et al. 2003). To achieve this goal, each AOR was observed for a total of 60 seconds, split evenly among the two dithered pointings of 30 seconds each. The limiting flux does not reach the IRAC confusion limit, and therefore confusion noise, which does not decrease as the square root of exposure time (Surace et al. 2005), is small (see Section 5.7 for more detail). The total observation time for the SpIES survey was ~820 hours (Table 3) split among the 154 AORs. Figure 3 demonstrates that the SpIES survey is both the largest *Spitzer* survey to date and reaches approximately to SWIRE depths, fulfilling two of the projects primary goals.

4. IMAGE REPROCESSING

Observations from *Spitzer* are downlinked to the *Spitzer* Science Center (SSC) where the raw images are sent through the "Level 1" processing pipeline. This pipeline corrects for known instrumental signatures in the images (dark subtraction, ghosting, and flatfielding) and flags possible cosmic ray hits. Additionally, the observed counts units (ADU) are converted into flux density units (MJy sr^{-1}), creating the Basic Calibrated Data (BCD) images (see Section 5 of the IRAC Handbook[23]). These BCD images are processed one $5.2' × 5.2'$ field at a time through a secondary pipeline to correct for other artifacts seen in IRAC images such as stray light (masking of scattered light from stars outside the array location) and column pulldown (a bright pixel causing a low background in the CCD array column; Figure 4), creating Corrected-BCD (cBCD) images (Section 6 of the IRAC Handbook) which were used to create stacked AORs (see Figure 2). A single cBCD image only covers one IRAC FOV; however, after accounting for the dithers and the two epochs, we have a total of four cBCD images which cover roughly the same region of the sky. The cBCD images are stacked to create the larger AOR mosaics using the SSC Mosaicing and Point-source Extraction (MOPEX[26]) software.

The MOPEX software was developed by the SSC specifically to process *Spitzer* BCD and cBCD images. This package contains many pipelines which can be used to process, stack, and extract sources from *Spitzer* images; however, we only relied on the mosaic pipeline to combine cBCD images onto a common frame. There are

[26] http://irsa.ipac.caltech.edu/data/SPITZER/docs/ dataanalysistools/tools/mopex/mopexusersguide/
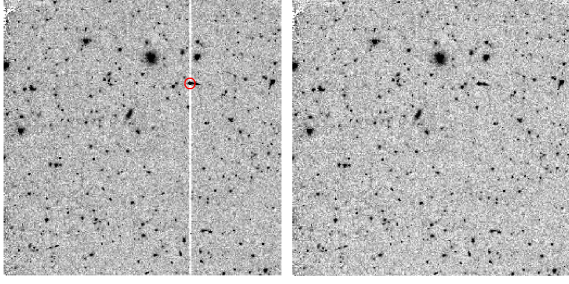
Fig. 4.— Left: Typical SpIES Level 1 BCD image from the SSC before corrections. The bright pixel (red circle) causes its whole column to drop to a low background value (causing the white line across the full array). Right: A cBCD image, which is the BCD image after it has been corrected for known signatures, such as the column pulldown in the left panel. The cBCD images are the size of an IRAC FOV ($5\rlap{.}'2\times5\rlap{.}'2$) and are mosaicked together to form the larger AORs seen in Figure 2. Both images are centered at (α, δ)=(32.611, -0.887) degrees.

TABLE 4
Parameter values for Mopex and SExtractor

Program	Parameter	Value
MOPEX	Fatal_Bitpattern	27392^a
SExtractor	DETECT_THRESH	1.25
SExtractor	DETECT_MINAREA	4
SExtractor	DEBLEND_NTHRESH	64
SExtractor	DEBLEND_MINCONT	0.005
SExtractor	PHOT_APERTURES^b	4.8, 6.4, 9.63, 13.6, 19.2, 40
SExtractor	PIXEL_SCALE	0.6
SExtractor	BACK_SIZE	64
SExtractor	BACK_FILTERSIZE	5
SExtractor	GAIN	4429.37, 3788.29^c
SExtractor	WEIGHT_TYPE	MAP_WEIGHT
SExtractor	WEIGHT_IMAGE	mosaic_cov.fits
SExtractor	WEIGHT_GAIN	Y
SExtractor	FILTER	Y
SExtractor	FILTER_NAME	default.conv

Note. — This is the list of parameters that were changed from the default MOPEX or SExtractor configuration files. These parameters were used in the stacking and source extraction of the SpIES images.
^{a}DCE_Status_Mask_Fatal_BitPattern with bits 8,9,11,13,14 are turned on.
^{b} The diameter of the aperture in pixels.
^{c}Gain values for the 3.6 μm, 4.5 μm detector. See Section 5.2 for more details

five stages of combination in the mosaic pipeline which transform a list of cBCD images to a full mosaic. First, an interpolation technique is run on the input images, determining the location of each pixel and forming a fiducial frame for the output image. Next, an outlier rejection script is run which flags or masks bad pixels from the final image. These flags are applied to the fiducial frame with a re-interpolation technique. Co-addition of pixel values is performed on tiles of pixels that make up the full image using a method defined by the user (for SpIES, pixels were co-added using a straight average). Finally, a script combines the tiles from the co-addition stage together to form a single image. Along with a combined image, MOPEX provides an option to output other datasets such as a coverage map and uncertainty map similar to those shown in Figure 2. The SSC also provides these images as "Level 2" post-BCD (pBCD) images which have been processed by MOPEX
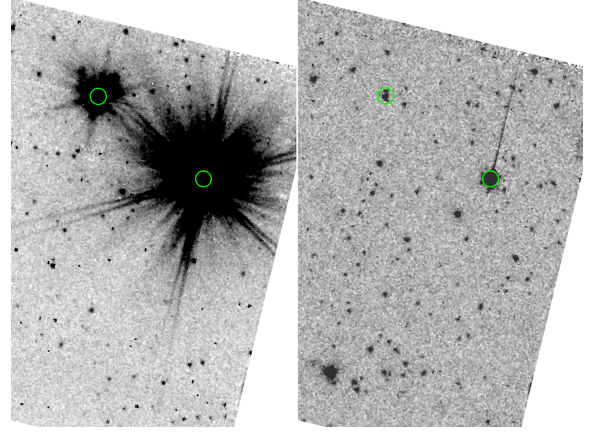

Fig. 5.— Shown on the left is an example of two bright stars in a $\sim3'\times4\rlap{.}'5$ cutout of a 3.6 μm cBCD (centered at (α, δ)=(34.464, -0.169) degrees). The image in the right panel is the next observation (centered at (α, δ)=(34.482, -0.247) degrees) showing the latent images from the bright stars in the previous observation (left panel). The green circles highlight the pixel location of the latent objects in IRAC from subsequent observations at different sky locations.

and thus can be used for source extraction and photometry; however, they are only single epoch images, thus do not achieve the full depth of our survey.

To achieve our full depth, we created images by submitting the cBCD images of the two overlapping epochs as well as their corresponding bit mask (bimsk) images and the uncertainty (cbunc) into MOPEX. The pipeline was run using the default parameters with the exception of the DCE_Status_Mask_Fatal_BitPattern (see Table 4) which tells MOPEX which pixels to mask in the final mosaic based on the bit value of those pixels in the input bit mask. For example, the 3.6 μm 'warm' IRAC images suffer from latent images[27] (typically after exposure to bright stars) which remain at the same pixel location on the detector for the next set of observations (see Figure 5). If left unchecked, these objects appear in a different sky location in the final image, and will be detected as individual sources. To prevent contamination in the final AOR, the SSC pipeline locates latent objects in each BCD, and flags the corresponding pixels in the bit mask[28] for that BCD. We then set the DCE_Status_Mask_Fatal_BitPattern (which reads the bit masks) to mask any objects that have that particular flag set in the final combined image (see Figure 6). Since latent objects do not appear in our final stacked images they are not present in our final catalogs.

The SSC-produced BCD, cBCD, and pBCD images, as well as all ancillary data images (uncertainty maps, coverage maps, etc.), are publicly available on the *Spitzer* Heritage Archive[29] (SHA) website. The images created by the SpIES team are publicly available (see Appendix A). There are a total of 231 images created by the SpIES team consisting of 154 individual epoch AOR mosaics and 77 combined epoch mosaics (stacking the two overlapping individual epoch images). Source extraction and

[27]http://irsa.ipac.caltech.edu/data/SPITZER/
docs/irac/iracinstrumenthandbook/63/
[28]http://irsa.ipac.caltech.edu/data/SPITZER/
docs/irac/iracinstrumenthandbook/44/#_Toc410728355
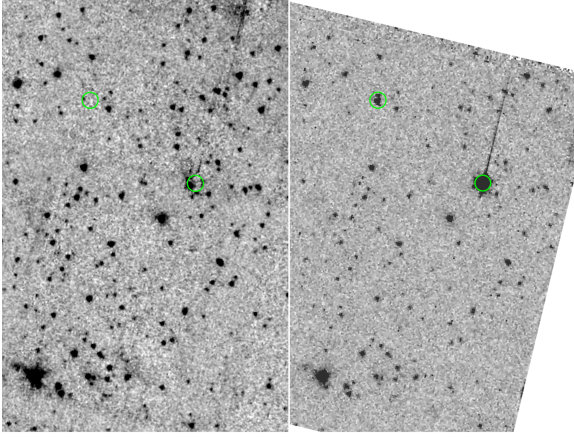[29]http://sha.ipac.caltech.edu/applications/Spitzer/SHA/

FIG. 6.— Here, the left panel shows a portion of the final stacked AOR image after sky matching to the right panel in Figure 5 (also the right panel of this figure) with the latent object locations outlined in green. Here we show that the latent objects in the cBCD (right panel) are masked in the final stacked image (left panel) because the latent image bits were turned off in the MOPEX processing pipeline (see Table 4), therefore, they do not appear in the final catalogs.

photometry were performed on each of these 231 images. The final catalogs were constructed by running our source extraction techniques on the 77 combined epoch AORs to take advantage of the full depth of SpIES. To illustrate the depth of SpIES, Figure 7 compares a region from a full-depth 4.5 micron AOR and the same region from *WISE* 4.6 micron ($W2$).
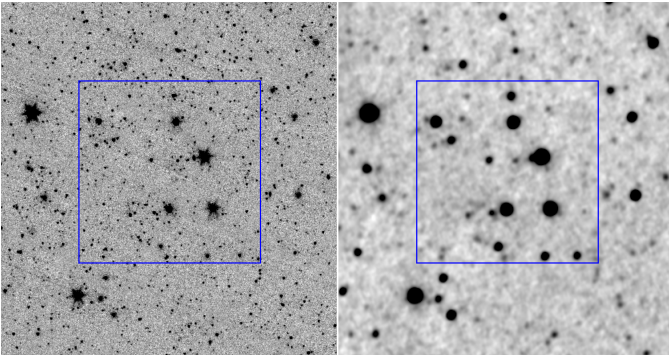

FIG. 7.— Comparison of a $\sim$100 arcmin^2 box of a SpIES 4.5 μm image and a 4.6 μm image which cover approximately the same central wavelength. 'Warm' IRAC 4.5 μm has a PSF of 2″02 compared to 6″4 for *WISE* 4.6 μm, allowing SpIES to resolve objects that are blended in *WISE*. Additionally, the superior depth of SpIES (AB magnitude of $\sim$22 in [4.5] compared to $\sim$18.8 in W2) yields more sources above the background ($\sim$1400 in the dual-band catalog) in the field shown compared to *WISE* ($\sim$350 in AllWISE). The blue boxes represent a single FOV of IRAC (5′2 × 5′2).

5. CATALOG PRODUCTION

5.1. *Source Extraction*

The SpIES catalogs were constructed by running Source Extractor (SExtractor; Bertin & Arnouts 1996) on each combined-epoch AOR mosaic, creating 77 AOR source catalogs for the 3.6 μm detections and 77 for the 4.5 μm detections. SExtractor uses a six-step source extraction routine which efficiently generates catalogs from

large images. First, a robust 3σ clipped background estimation is performed on the entire image, which has been inspected through an output background map. This step is followed by a thresholding algorithm which extracts objects at a certain, user-specified standard deviation above the background. SExtractor then runs a deblending routine to separate potentially blended sources, filters the image using an input filtering routine, and performs photometry on detected sources within user specified apertures. Finally, SExtractor attempts to classify objects as point-like (stars) or extended (galaxies) based on the input pixel scale and stellar FWHM of the survey.

Each step is controlled through an input configuration file and an output parameter file. There are a variety of parameters that can be changed in the configuration file, some of which can significantly change the source extraction results. The final configuration file was a mix of parameters tested on the SpIES images and parameters adopted from previous programs such as the SERVS (Mauduit et al. 2012) and SWIRE (Lonsdale et al. 2003) surveys. Table 4 lists the configuration parameters used in our processing.

Previous *Spitzer* surveys also used the coverage map created in MOPEX as a weighted image during source extraction. These images hold information about the number of times a particular pixel in the AOR was observed, which is related to the effective exposure time at each pixel. Since the signal-to-noise ratio of an object increases with the square root of exposure time in these data, the coverage maps assign pixels with more coverages (i.e., longer exposures) a higher weight. Following this convention, the coverage maps were input as weight maps, converted into a variance map by SExtractor through the inverse relationship between weight and variance, and scaled to an absolute variance map created internally by SExtactor. This processing is also controlled through the input configuration file during source extraction.

SExtractor can be run in either single-detection mode, which performs source detection, aperture definition, and photometry on the same image, or dual-detection mode, which finds sources and defines apertures on a first input image (for example, a 3.6 μm AOR) and performs photometry on a second input image (the same AOR observed using the 4.5 μm detector). All of the SpIES AOR mosaics were run in single-detection mode, creating 77 double-epoch catalogs for each channel. Full-area, single-channel catalogs were made by concatenating the 77 individual AOR catalogs using the Starlink Tables Infrastructure Library Tool Set (STILTS)[30]. These single-channel catalogs are designed to contain a single row for each object in the SpIES survey, so when two objects match within 1″ between two AORs (which is possible since the AORs overlap) we report the average position, the weighted average of the flux density values (using the errors as weights), and the errors added in quadrature in a single row in the catalog (the overlapping regions between AORs account for $\sim$10% of the total survey area). Though we report objects that are detected 5σ above the calculated background, many objects have a signal-to-noise (S/N) less than less than 5 due to Poisson noise.

Photometry on SpIES sources was performed in six cir-

[30]http://www.star.bris.ac.uk/~mbt/stilts/

Band	1″4	1″9	2″9	4″1	5″8
3.6 μm	0.584	0.732	0.864	0.911	0.950
4.5 μm	0.570	0.713	0.865	0.906	0.946

NOTE. — Measured aperture corrections for SpIES objects with good flags matched to the 2MASS point source catalog. These corrections are nearly identical to those used in SERVS (Mauduit et al. 2012) for identical aperture radii.

cular apertures of radii 1″4, 1″9, 2″9, 4″1, 5″8, and 12″, reported as diameter in pixels in the SExtractor configuration file in Table 4. The first five apertures (which are the same size as the SERVS apertures) contain only a fraction of the light from each source, while the sixth contains "all" the light from the source (see Section 4.11 of the IRAC Handbook[23]). The aperture correction factors in Table 5 are measured for the SpIES survey for objects with good flags (discussed in more detail in Section 5.3) matched to the 2MASS Point Source Catalog (PSC) to ensure that measurements were performed on point sources only. We then took the ratio of the light in the smaller apertures to the light in the largest aperture, made a histogram of the resulting factors for each aperture, and fit a Gaussian to that histogram to measure the peak and spread of the distribution. The location of the peak of the Gaussian was used as the correction factor. The corrections measured for SpIES differ by less than 1% of those used in SERVS (Mauduit et al. 2012) for the exact same aperture radii. Aperture corrections are useful for finding faint objects with a radius much less than the large 12″ radius aperture, because in these cases the background noise in the aperture would dominate the object. We primarily use the 1″9 radius aperture for analysis in the following sections as it corresponds to a $\sim$70% curve of growth correction (the curve showing how the flux density ratio changes with aperture size) in both channels.

After objects are extracted from the images, the surface brightness values are converted from the *Spitzer* image unit of MJy sr^{-1} to flux densities (μJy) per pixel as using the following conversion:

$$\frac{\text{MJy}}{\text{sr}} \left(10^{12} \frac{\mu \text{Jy}}{\text{MJy}} \right) \left(\frac{\pi \text{rad}}{180°} \right)^2 \left(\frac{1°}{3600″} \right)^2 \left(\frac{0″6}{\text{pixel}} \right)^2$$

such that,

$$1 \text{MJy steradian}^{-1} = 8.46 \mu \text{Jy pixel}^{-2} \qquad (1)$$

where we multiply by the SpIES pixel size of 0″6, which is half of the IRAC pixel size due to the image dithering.

This correction factor in Equation 1 was applied to each pixel in the image which, when summed in an aperture, yields the total flux density of the source. This value was divided by the appropriate aperture correction from Table 5 to produce the final flux density value for the objects in the catalogs.

5.2. *Photometric Errors*

Photometric errors were computed using SExtractor and are reported in the catalog (see Table 4). According to Section 10.4 of the SExtractor manual, the 1σ photometric errors are computed via

$$\sigma_{\text{source}} = \sqrt{A\sigma_{rms}^2 + \frac{F}{g}}, \qquad (2)$$

where A is the measurement area in pixels, σ_{rms} is the background RMS value of each pixel, F is the background-subtracted source count value in the measurement aperture, and g is the detector gain. This expression is simply the rms background added in quadrature with the Poisson noise. SExtractor assumes that the signal in the input images is in units of counts, typically a Digital Number (DN) which is the number of photons counted scaled by the detector gain value. *Spitzer* images, however, are converted to physical units during "Level 1" processing (as mentioned in Section 4). Many previous surveys which have used SExtractor to compute photometric errors exclude the Poisson noise and only report the rms background error, which is also the SExtractor default if no gain is supplied. For bright objects, Poisson noise dominates, and thus using the background error alone dramatically underestimates the true error in the reported flux density. Here we compute and report the full photometric errors from SExtractor for the SpIES survey, correcting for the *Spitzer* image flux units such that both background and Poisson noise are included in the error estimate. Indeed the majority of the sources in our "5σ catalog" (Section 5.1) will have true soure S/N < 5 (and more typically $\sim$2-3).

To properly incorporate *Spitzer* data into Equation 2, we first examine its fundamental components: the noise due to the background and Poisson counting noise. In order to compute the background noise, SExtractor first creates a background map (as discussed in Section 5.1) and a background rms map. The background rms map is constructed by calculating the squared rms deviation of each pixel in the background map from the local mean background (whose size is defined by the BACK_SIZE parameter in Table 4). The background noise is simply the sum of the background rms pixels inside a given aperture (where $A\sigma_{rms}^2$ in Equation 2 is synonymous with the sum over the background rms).

Poisson noise is the discrete counting error which occurs when performing photometry on a source. SExtractor performs photometry on an object inside of an aperture by counting the total pixel value and subtracting the background as follows:

$$F = C - B \qquad (3)$$

where F is the background-corrected count value of an object, B is the sum of the local background value in the aperture, and C is the total number of counts in an aperture. Assuming the pixel values in the measurement aperture are uncorrelated (which presents a separate problem that is discussed later in this section), then the error in F can be calculated using the propagation of error equation:

$$\sigma_F^2 = \left(\frac{\delta F}{\delta C} \right)^2 \sigma_C^2 + \left(\frac{\delta F}{\delta B} \right)^2 \sigma_B^2 \qquad (4)$$

where σ_C and σ_B are the Poisson errors of the total number of counts and background respectively. Taking the

derivatives of Equation 3 and inserting them into Equation 4, we obtain:

$$\sigma_F^2 = \sigma_C^2 + \sigma_B^2. \qquad (5)$$

The number of electrons measured, the number of counts reported, and the gain are related by:

$$\#e^- = g \times F \qquad (6)$$

which has an uncertainty,

$$\sigma_{\#e^-}^2 = g^2 \times \sigma_F^2. \qquad (7)$$

Poisson statistics dictate that the variance of a discrete value (in this case electron number, $\sigma_{\#e^-}^2$) is equal to that value (the number of electrons counted). We therefore relate the number of electrons to the digital count in Equation 6 and obtain that the Poisson error for a digital count is:

$$\sigma_F^2 = \frac{\#e^-}{g^2} = \frac{g \times F}{g^2} = \frac{F}{g}. \qquad (8)$$

This Poisson error (which must have the digital count unit) is the second term in Equation 2, and is added in quadrature with the rms background error to generate the total source error found in Equation 2.

Spitzer images and SExtractor use two different definitions of the gain. SExtractor is programmed to interpret this parameter as purely the detector gain (which has units of electrons per digital count) whereas *Spitzer* images have a definition of gain that includes the conversion factor between counts units and physical units. Even though SExtractor expects an image in counts units, we can input *Spitzer* images by incorporating this conversion factor in the gain parameter according to the equation:

$$G = \frac{N \times g \times T}{K} \qquad (9)$$

where N is average number of coverages estimated from each AOR coverage map, g is the detector gain of 3.7 $e^- (DN)^{-1}$ for the $3.6\,\mu$m detector and 3.71 $e^- (DN)^{-1}$ for the $4.5\,\mu$m detector, T is exposure time for one coverage, and K is the conversion factor from digital to physical units found in either the cBCD header or the Warm IRAC Characteristics webpage[31]. For the SpIES images, we calculated the weighted gain, G, to be 4429.37 $e^- (\mathrm{MJy\,sr^{-1}})^{-1}$ at $3.6\,\mu$m and 3788.29 $e^- (\mathrm{MJy\,sr^{-1}})^{-1}$ at $4.5\,\mu$m; these values were used in the SExtractor configuration file for source extraction and error estimation. In short, replacing the detector gain, g, with the weighted gain, G, in Equation 2 allows a proper determination of both the background and Poisson noise when applying SExtractor to images that have been converted to physical units.

After the gain parameter is replaced, applying simple unit analysis to Equation 2 shows that the errors have the same unit as the input image (in this case MJy sr^{-1}). We therefore need to convert the errors from image units of MJy sr^{-1} to μJy using Equation 1 in the same way as we did for the flux density values. The error analysis was also done inside apertures of varying radii and therefore

also must be aperture corrected by dividing by the values in Table 5.

Finally, Equation 2 is based on the assumption that the pixels in the images are uncorrelated, which simplifies the SExtractor error calculation. In reality, the SpIES images will have cross correlation terms due to processes such as dithering, reprojection, and stacking, which correlate the count value in overlapping pixels. Since SExtractor does not take correlated noise into account, we corrected the values by multiplying the errors by a factor of two (the ratio of the pre-processed image pixel scale of $1''2$ to the post-processed pixel scale of $0''6$), which accounts for the pixels being sampled twice due to the two dithers in the survey. Although the errors are slightly adjusted to account for oversampling, they should still be considered as lower limits on the true error in each aperture since there are other contributions to the correlated noise in each pixel for which we do not correct (i.e., noise pixels). Various methods to estimate the survey depth are presented in Section 5.6, one of which uses the output photometric errors a direct measure.

5.3. *SpIES Source Catalogs*

Using the parameters in Table 4 and employing the techniques discussed in previous sections, we generated the SpIES 5σ detection catalogs. Here 5σ refers not to objects with a ratio of flux density to flux density error of greater than five, but rather to objects whose flux density is greater than five times the background. This limit is found by taking the product of the DETECT_MINAREA (minimum number of adjacent pixels to make a source) and DETECT_THRESH (number of standard deviations above the background per pixel) parameters (see Table 4 for reference). In fact, the majority of these objects have a S/N of $\sim$2-3, due in large part to the addition of the Poisson noise as shown in Section 5.2.

With this release, we provide three separate detection catalogs: a $3.6\,\mu$m-only detection catalog which contains $\sim$6.1 million objects that are only detected at $3.6\,\mu$m, a $4.5\,\mu$m-only detection catalog containing $\sim$6.6 million objects only detected at $4.5\,\mu$m, and a dual-detection catalog containing $\sim$5.4 million sources, comprised of the sources detected at the same positions in both bands. These catalogs were constructed by extracting sources from the $3.6\,\mu$m and $4.5\,\mu$m AORs separately to generate full object catalogs for each channel. We then matched these two single-band catalogs using a matching radius of $1''3$ (as determined by the Rayleigh criterion), which maximized the number of true matches and minimized the false detections between the two channels to create our combined dual-band catalog. The objects that did not match remained in the single band catalogs. Due to the offset between the detectors in IRAC, there were $\sim$600,000 objects in $3.6\,\mu$m without coverage in $4.5\,\mu$m and $\sim$600,000 objects in $4.5\,\mu$m without coverage in $3.6\,\mu$m. These objects, however, are retained in their respective single band catalogs. As the majority of the objects in the single-band catalogs have S/N$\sim$2-3, it is perhaps not surprising that they are detected in only one band. However, included among these will be transient objects and mid-infrared/optical dropouts, which are clearly of interest, in addition to spurious sources, which clearly are not. Thus, we recommend using the high reliability flags for the most reliable objects in each

---

[31] http://irsa.ipac.caltech.edu/data/SPITZER/docs/
irac/warmimgcharacteristics/

TABLE 6
SpIES catalog columns

Column Name	Description
RA_ch1	J2000 RA position at $3.6\,\mu m$
DEC_ch1	J2000 DEC position at $3.6\,\mu m$
FLUX_APER_1_ch1	$3.6\,\mu m$ flux density, $1\rlap{.}''44$ radius
FLUX_APER_2_ch1	$3.6\,\mu m$ flux density, $1\rlap{.}''92$ radius
FLUX_APER_3_ch1	$3.6\,\mu m$ flux density, $2\rlap{.}''89$ radius
FLUX_APER_4_ch1	$3.6\,\mu m$ flux density, $4\rlap{.}''08$ radius
FLUX_APER_5_ch1	$3.6\,\mu m$ flux, $5\rlap{.}''76$ radius
FLUX_APER_6_ch1	$3.6\,\mu m$ flux density, $12''$ radius
FLUXERR_APER_1_ch1	$3.6\,\mu m$ flux density error, $1\rlap{.}''44$ radius
FLUXERR_APER_2_ch1	$3.6\,\mu m$ flux density error, $1\rlap{.}''92$ radius
FLUXERR_APER_3_ch1	$3.6\,\mu m$ flux density error, $2\rlap{.}''89$ radius
FLUXERR_APER_4_ch1	$3.6\,\mu m$ flux density error, $4\rlap{.}''08$ radius
FLUXERR_APER_5_ch1	$3.6\,\mu m$ flux density error, $5\rlap{.}''76$ radius
FLUXERR_APER_6_ch1	$3.6\,\mu m$ flux density error, $12''$ radius
FLUX_AUTO_ch1	Total $3.6\,\mu m$ flux density
FLUXERR_AUTO_ch1	Total $3.6\,\mu m$ flux density error
FLAGS_ch1	$3.6\,\mu m$ SExtractor Flags
CLASS_STAR_ch1	$3.6\,\mu m$ morphology classification
FLAG_2MASS_ch1	$3.6\,\mu m$ object near a bright star
COV_ch1	Number of cBCD coverages
HIGH_REL_ch1	Most reliable objects with good flags
RA_ch2	J2000 RA position at $4.5\,\mu m$
DEC_ch2	J2000 DEC position at $4.5\,\mu m$
FLUX_APER_1_ch2	$4.5\,\mu m$ flux density, $1\rlap{.}''44$ radius
FLUX_APER_2_ch2	$4.5\,\mu m$ flux density, $1\rlap{.}''92$ radius
FLUX_APER_3_ch2	$4.5\,\mu m$ flux density, $2\rlap{.}''89$ radius
FLUX_APER_4_ch2	$4.5\,\mu m$ flux density, $4\rlap{.}''08$ radius
FLUX_APER_5_ch2	$4.5\,\mu m$ flux density, $5\rlap{.}''76$ radius
FLUX_APER_6_ch2	$4.5\,\mu m$ flux density, $12''$ radius
FLUXERR_APER_1_ch2	$4.5\,\mu m$ flux density error, $1\rlap{.}''44$ radius
FLUXERR_APER_2_ch2	$4.5\,\mu m$ flux density error, $1\rlap{.}''92$ radius
FLUXERR_APER_3_ch2	$4.5\,\mu m$ flux density error, $2\rlap{.}''89$ radius
FLUXERR_APER_4_ch2	$4.5\,\mu m$ flux density error, $4\rlap{.}''08$ radius
FLUXERR_APER_5_ch2	$4.5\,\mu m$ flux density error, $5\rlap{.}''76$ radius
FLUXERR_APER_6_ch2	$4.5\,\mu m$ flux density error, $12''$ radius
FLUX_AUTO_ch2	Total $4.5\,\mu m$ flux density
FLUXERR_AUTO_ch2	Total $4.5\,\mu m$ flux density error
FLAGS_ch2	$4.5\,\mu m$ SExtractor Flags
CLASS_STAR_ch2	$4.5\,\mu m$ morphology classification
FLAG_2MASS_ch2	$4.5\,\mu m$ object near a bright star
COV_ch2	Number of cBCD coverages at $3.6\,\mu m$
HIGH_REL_ch2	Most reliable objects with good flags

Note. — Column descriptions for the three SpIES catalogs. The $3.6\,\mu m$-only and $4.5\,\mu m$-only catalogs are built in exactly the same manner without the columns from the other channel. All flux density and flux density error columns in this catalog have been converted from MJy sr^{-1} to μJy pixel^{-1} using Equation 1, and the first five apertures in each channel have been aperture corrected using the values in Table 5.

catalog (described below).

These catalogs were constructed from the combined epoch AORs, and thus reach the full depth achievable by the SpIES survey. As also noted in the previous section, each row in the catalogs contains a unique source. The columns hold information about the astrometric and photometric values for each source, the flags that were generated during source extraction, and several binary columns which have various meanings (see Table 6). The three catalogs are structured in exactly the same way, the only difference being whether or not the object in the catalog is matched between the two channels. A user desiring *all* the $3.6\,\mu m$ detections can electronically concatenate the $3.6\,\mu m$-only and the dual-band catalogs without any changes to the files.

Each row in the catalog contains information about a unique source at a particular J2000 RA and DEC position, which was determined by SExtractor, as reported

TABLE 7
Sextractor flags

Bit Value	Description
1	The object has neighbors, that significantly bias the photometry, or bad pixels.
2	The object was originally blended.
4	At least one pixel is (nearly) saturated.
8	The object is truncated (close to image boundary).
16	Aperture data are incomplete or corrupted.
32	Isophotal data are incomplete or corrupted.
64	A memory overflow occurred during deblending.
128	A memory overflow occurred during extraction.

Note. — All of the extraction flags from SExtractor. The first five flags are the most common for SpIES as these pertain to issues in source extraction. The last three do not appear in the SpIES data since there are no isophotal aperture measurements and a sufficient amount of memory was allocated for extraction.

in the first two columns (both channel positions are reported for matched objects). These positions have been corrected for a slight offset when compared to SDSS point sources (see Section 5.4 for more details). The subsequent twelve columns report the flux density values from the six different measurement apertures used in source extraction along with their respective errors. Aperture-corrected flux density values are reported in these columns (except for aperture 6 which is not corrected) and surface brightness units (MJy sr^{-1}) are converted to flux densities (μJy) using Equation 1. Additionally, the errors have been adjusted in the manner described in the previous section. The next two columns (FLUX_AUTO and FLUXERR_AUTO) report the flux density and flux density error in apertures whose size and shape are determined by SExtractor to contain the total flux density from a source. These last two values have been converted to flux densities using Equation 1; however, they are not aperture corrected.

The extraction flags are reported in the next two columns (see Table 7 for more information). Since source extraction was performed on an individual AOR basis, the sources on the edges of AORs have the potential to be detected twice, due to the overlap between AORs, and thus both flags were retained (however there is only one row entry in the catalog for overlapping objects). Sources that do not overlap have a flag value in the first column and were given a value of -999.0 in the second column to make it clear that this source was detected in only one AOR. The SExtractor stellar class is reported in the CLASS_STAR column which is a probability that ranges from 0 to 1 and indicates whether an object is resolved (values closer to 1) or extended (values near 0). If the object was detected twice due to the overlap of the AORs, the average value is given in the catalog. We find this measurement to be most reliable for objects with magnitudes brighter than 20.5 ($\sim$1.7 million at $3.6\,\mu m$ and $\sim$1.5 million at $4.5\,\mu m$ in the dual-band catalog), with $\sim$40% classified as resolved (CLASS_STAR ≥ 0.5) and $\sim$60% as extended (CLASS_STAR ≤ 0.5) in both bands (see Figure 8).

Following the SExtractor output columns are a series of flags created after source extraction. The FLAG_2MASS column is a binary flag indicating whether a source is detected within a particular radius (defined by Table 8)
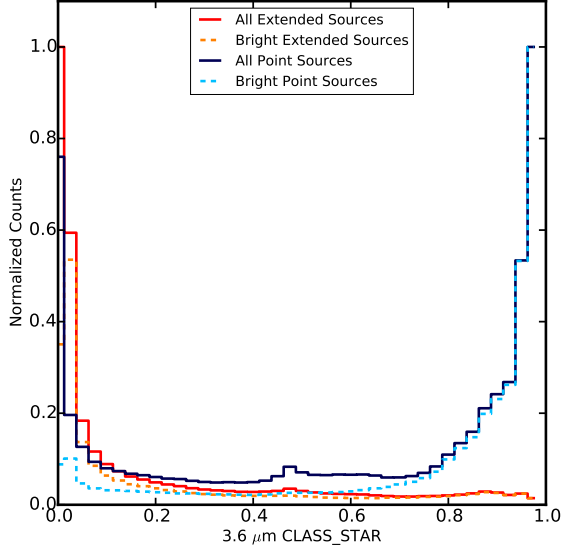
2MASS (K_s-Magnitude)	Radius ($''$)
≥ 12	0
$12 - 10$	40
$10 - 9.0$	60
$9.0 - 8.0$	90
$8.0 - 7.0$	120
$7.0 - 6.0$	150
≤ 6.0	180

NOTE. — Objects that fall within the radii given are flagged as bright star contaminants. These values are empirically determined by making K_s-magnitude cuts on 2MASS stars and studying figures like Figure 9 and Figure 10. The K_s-magnitudes are computed in Vega magnitudes.
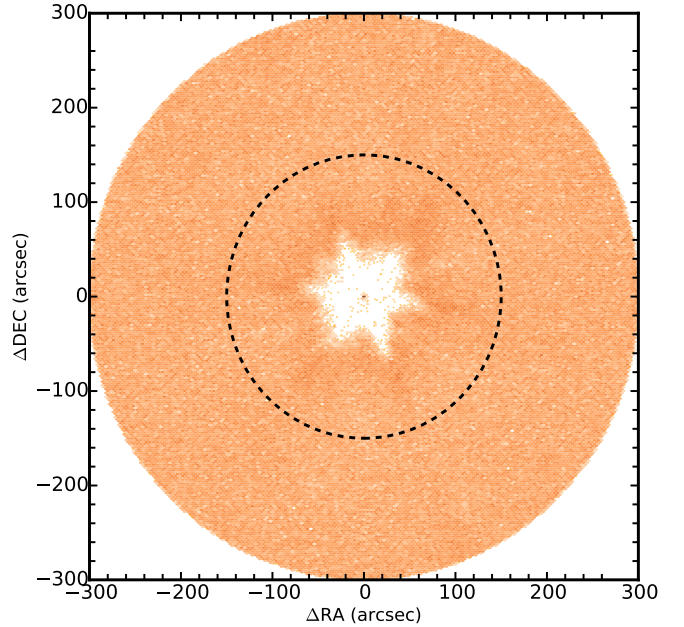
FIG. 8.— Comparisons of the CLASS_STAR parameter at $3.6\,\mu m$ for objects matched to SDSS sources. We show the distribution for all optically extended sources (red) and all optical point sources (dark blue). Optically extended sources peak at CLASS_STAR~ 0, while optical point sources peak at ~ 1; however there is a small peak at 0.5 implying that SExtractor could not differentiate between point or extended. For bright objects ($[3.6] \leq 20.5$), however, the extended (orange dashed) and point (light blue dashed) sources still peak at 0 and 1, respectively, but there are far fewer confused classifications. A similar trend occurs for the objects detected at $4.5\,\mu m$.

around a bright star in the 2MASS point source catalog (PSC). Inside this radius there is an excess of artificial sources due to artifacts from the bright star (e.g., diffraction spikes). Flags are assigned to objects near 2MASS stars with K_s-magnitude brighter than 12 (Vega magnitude), where the radii range from $40''$ at the faint end to $180''$ at the bright end. For comparison, the radii used for the SWIRE survey range from $10''$ at the faint end to $120''$ at the bright end using similar (but not the same) K_s-magnitude cuts (see Surace et al. 2005).

The SpIES bright-star flagging radii were empirically determined by cutting the 2MASS PSC into a series of K_s-band magnitude ranges and matching their positions to all SpIES objects within $300''$. We then overlay the positions of all of the stars in a K_s-magnitude bin along with their SpIES matches onto a common coordinate frame and determine the radius which encapsulates the over-dense region around the star. Figure 9 shows the result of stacking $6 \leq K_s \leq 7$ Vega magnitude stars and their matches on a coordinate frame. The radial profile plot is presented in Figure 10 which clearly shows an excess of detections near bright stars. Objects that fall within the radii in Table 8 are given a value of 1 in the catalog to indicate that the source is potentially spurious, and the central star itself is given a value of 2. Using the radii in Table 8, we compute the area lost when rejecting such sources is ~ 5 deg^2 for both bands (which is $\sim 5\%$ of the dual-band catalog area).

We report the number of cBCD coverages (from the coverage maps shown in Figure 2) at the centroid position of each source in the COV columns. Since AORs overlap, we give an array of two values where, if the object does

FIG. 9.— The 335 stacked $6 \leq K_s$-magnitude≤ 7 stars matched to SpIES within $300''$. The black dashed circle shows the radius out to which we flag objects as potentially contaminated.

not overlap, we report -999.0 (similar to the extraction flags). For the most reliable detection, we recommend using objects which have greater than two coverages in either entry of the reported array.

Finally, we have created a high reliability column which we recommend for users whose science requires that the objects be robust sources and/or have robust photometry. There are three values in this column indicating whether a source is a real object (flagged with a value of 1 or 2), has good photometry (flagged with a value of 2), or does not satisfy the following good flag conditions (flagged with a 0). To be regarded as a real source, the SExtractor flags must be less than or equal to 4, the objects must have flag 0 or 2 in the FLAG_2MASS col-
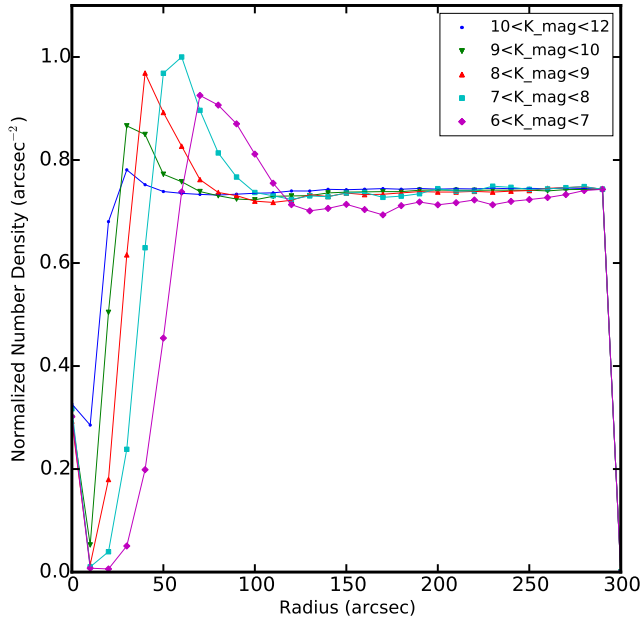
FIG. 10.— Radial profiles of the number density of objects within $300''$ of 2MASS stars in magnitude ranges given in Table 8, showing how the number density of detected objects around bright stars changes as a function of distance from the center of the star. The peak in these curves is the over-dense region where there are spurious detections due to artifacts such as diffraction spikes. We cut at the radius where the curves approach a constant value of number density for each magnitude.

umn, and there has to be greater than or equal to two coverages for each source. For an object to have good photometry, we further require that the SExtractor flags be less than or equal to 0 or equal to 2 (i.e., -999.0, 0, and 2), FLAG_2MASS must be 0, and it must satisfy the same coverage conditions as before. These flags cause holes in the coverage across the survey, thus changing the total coverage area. In total, SpIES has ~115 deg^2 of coverage in both wavelengths, of which, each band covers ~107 deg^2 (since there is an offset in the arrays discussed in Section 3) and there is ~100 deg^2 of dual-band coverage. For HIGH_REL>0, the areas are ~106 deg^2, ~101 deg^2, and ~94 deg^2, while for HIGH_REL=2, the areas drop to 105 deg^2, ~100 deg^2, and ~89 deg^2. While our catalog only includes sources more than 5σ above the background, full error analysis means that individual objects can have S/N (as computed by FLUX/FLUXERR) less than 5. Some users may want to apply a cut on S/N in addition to using the HIGH_REL flag. For a cut at S/N>3 and HIGH_REL>0, we retain ~1.4, ~3.9, and ~1.4 million objects in the $3.6\,\mu$m-only, dual-band, 4.5μm-only, respectively.

5.4. Astrometric Reliability

The astrometric reliability of SpIES was tested by comparing the centroid positions of point sources in SDSS with matched objects in the SpIES dual-band catalog (within $2''$). We found the difference in position for objects which have good flags in SDSS (BITMASK=0 and PHOTOMETRIC=1), are bright in the r-band ($r \leq 21$), and have good flags in SpIES (HIGH_REL=0). Fitting a Gaussian to the histograms in Figure 11, we find that the
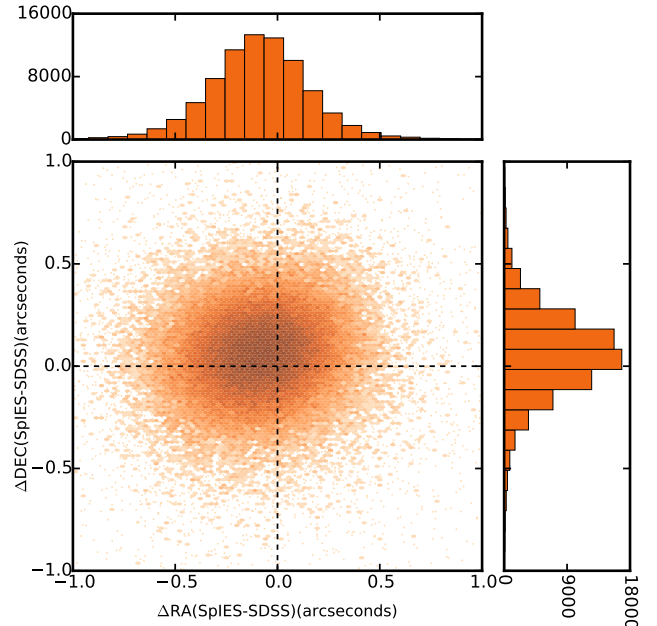

FIG. 11.— Comparison of the SpIES and SDSS astrometry for matched point sources with good flags in both surveys. Darker regions and histograms show the approximate point density. We use the mean offsets of the ΔRA and ΔDEC distributions shown here to correct the SpIES astrometry.

mean difference in RA is $-0''112 \pm 0''0008$ and in DEC is $0''0372 \pm 0''0006$ for these objects. These values were then used to correct the astrometry in all three SpIES catalogs. We also matched the SpIES data with the 2MASS PSC and found that the mean astrometric offsets (ΔRA$= -0''086 \pm 0''0006$ and ΔDEC$= 0''011 \pm 0''0005$) are slightly smaller than the calculations from SDSS, however confirm the direction of the SpIES positional shifts.

To see if the astrometric offset changes with brightness, we performed the same measurement using the SDSS matched point sources for bright and faint sources in [4.5]. We find that the astrometric offsets to be rather consistent both for faint ([4.5] ≥ 20) objects with ΔRA$= -0''112 \pm 0''0009$ and ΔDEC$= -0''0370 \pm 0''0007$ and for bright objects ([4.5] ≤ 20) with ΔRA$= -0''112 \pm 0''0014$ and ΔDEC$= -0''0376 \pm 0''0012$. Regardless of brightness, with the $0''6$ pixel scale of the SpIES images, the astrometric offset is approximately one sixth of a pixel, which is similar to the values calculated in Ashby et al. (2009) where the SDWFS astrometry was compared to 2MASS.

5.5. Completeness and Number Counts

To estimate the completeness of our detection strategy, we employed a Monte Carlo approach where we simulated 15,000 sources (about 4% and 6% of the total number of sources) with random magnitudes between 14.5 and 28 at random positions on each AOR. The simulated sources were allowed to fall anywhere on the image, including on top of other sources, thus our completeness estimates are robust against confusion noise (see Ashby et al. 2013). Each source was modeled as a point source, having a Gaussian profile with the same FWHM as IRAC. We ran SExtractor on these simulations in the exact manner described in Section 5.1 and

matched to a file containing the position and magnitude for each source. The tables of recovered sources for each AOR were then concatenated as before to cover the full footprint of SpIES. Number counts as a function of magnitude were plotted for both the recovered object catalog and the full simulated source catalog and the ratio of counts in each bin was calculated to estimate the completeness of the survey. Figure 12 presents the SpIES completeness curve for each passband, and the 90, 80, and 50 percent completeness values are quoted in Table 9. These measurements are performed for the entire survey field, however SpIES spans a wide range in right ascension. We therefore evaluated the completeness at different ranges in right ascension to evaluate how it changes with position. We found that the differences between the completeness curves that were computed for the full survey in Figure 12 and the curves computed at different locations in the SpIES survey were not significantly different, and that the differences in the 90, 80, and 50 percent complete values do not exceed ∼0.15 magnitudes for both the 3.6 μm and 4.5 μm measurements.

Differential number count histograms provide a visual representation of the distribution of objects of different magnitudes in a survey. They can be used to approximate the number of particular objects (stars, quasars, galaxies, etc.) that should be detected in the survey and can provide a rough estimate of the depth of the survey. The number of objects per square degree per magnitude is plotted as a function of flux density and AB magnitude in Figure 13 for SpIES objects detected in each band that satisfy the condition HIGH_REL>0. Shown for comparison are the differential number counts from SSDF (Ashby et al. 2013), which has a similar depth as SpIES, along with counts from the SERVS XMM field (Mauduit et al. 2012) and the S-COSMOS survey (Sanders et al. 2007), both of which are deeper than SpIES. Additionally, we show the contribution of Milky Way stars to these number counts estimated using the DIRBE Faint Source Model (FSM; Arendt et al. 1998; Wainscoat et al. 1992). At the bright end, the four surveys and the FSM all tend to align and follow a similar linear trend, indicating that the bright objects in the SpIES catalog are well represented and are mostly attributed to light in the Milky Way. The "turn over" in these histograms indicates the location of the approximate value of the depth of the survey. This is, however, an imperfect measure of the depth since artifacts tend to increase at the faint limits of a survey, resulting in more counts at fainter magnitudes.

The SpIES differential number counts in Figure 13 are computed for the full footprint of the survey. The spatial extent of SpIES is large enough, however, that it intersects the Galactic plane at different angles which has a small effect on the number counts, particularly for faint objects ($20 \leq \mathrm{AB} \leq 22$). For this reason the FSM, which is calculated for only a small area on the sky, is represented by a grey shaded region. To test the effect of Galactic latitude on the number counts, we split SpIES into different regions at different Galactic latitudes ($0 \leq b \leq 15$, $15 \leq b \leq 30$, and $b \geq 30$) and recompute the number counts as a function of magnitude. We find fewer faint objects are recovered for low Galactic latitudes, however as we look further off of the Galactic plane the SpIES number counts become consistent with those for surveys of similar depth (i.e. SSDF).

5.6. Depth

There are multiple ways of determining the depth of a survey, and the optimal value to use depends on the intended application. We computed the depth in four different ways for our analysis. First, we find the magnitude where the completeness curves turn over (see Figure 12). Object detection declines rapidly at this magnitude, making it a useful indicator of survey depth. An estimate of the limiting magnitude using the 90th percentile of completeness for simulated sources is [3.6]=21.75 and [4.5]=21.90. We report the 90, 80, and 50 percent complete values in Table 9.

Secondly, we can estimate the 5σ and 2σ depths by plotting the magnitude error as a function of magnitude (see Figure 14). From Figure 14 we determine the magnitude value where the outer edge of the curve reaches a magnitude error of ∼0.2 to obtain the 5σ magnitude limit. For SpIES, this limit occurs at [3.6]=21.93 and [4.5]=22.00, which corresponds to flux density values of 6.13 μJy and 5.75 μJy, respectively.

Another method to estimate depth is to perform empty aperture photometry where we placed random apertures on the images and performed source extraction in each aperture. We then made a histogram of the measurements with negative flux density values in the 1″.9 aperture in an attempt to eliminate contamination from sources to the background measurements. We then fit a Gaussian curve to the data to find the standard deviation in the background, σ_{bg}, across the SpIES field. We find that the $5\sigma_{bg}$ measurements are 8.14 μJy at 3.6 μm and 7.55 μJy at 4.5 μm. While this does not directly measure the depth to which we observe, it is a robust measurement of the noise in the data, including confusion noise since the apertures were randomly placed on our images.

Finally, we use the the predicted limits produced by the SENS-PET[32] tool. This estimate calculates the 5σ point source depth given the background level of the survey (depending on the survey location), the exposure time, and number of repeat exposures over a single area. The SpIES depth is estimated at 6.15 μJy at 3.6 μm and 7.2 μJy at 4.5 μm using a medium background, an exposure time of 30 seconds, and four overlaps in the 'Warm IRAC Parameters' section. This tool appears to calculate depths that are shallower than the measured depths; however, it is useful for making robust comparisons to other survey fields (for example, see Figure 13).

There are multiple reasons for the slight differences between the prediction from SENS-PET and our measurements. First, the noise estimates previously discussed in Section 5.2 should be considered a lower limit on the error and therefore the signal-to-noise ratios may be overestimated. Second, an overlap value of 4.0 was inserted into the SENS-PET calculator, whereas in reality the overlap of the SpIES BCD images averages to a value of ∼4.5 per pixel. The more coverage, the deeper the observations, so the theoretical value will be slightly brighter than reality. Finally, there could be a disparity between the background model used in SENS-PET and the measured background from the SpIES AORs, which could lead to a difference in the depth.
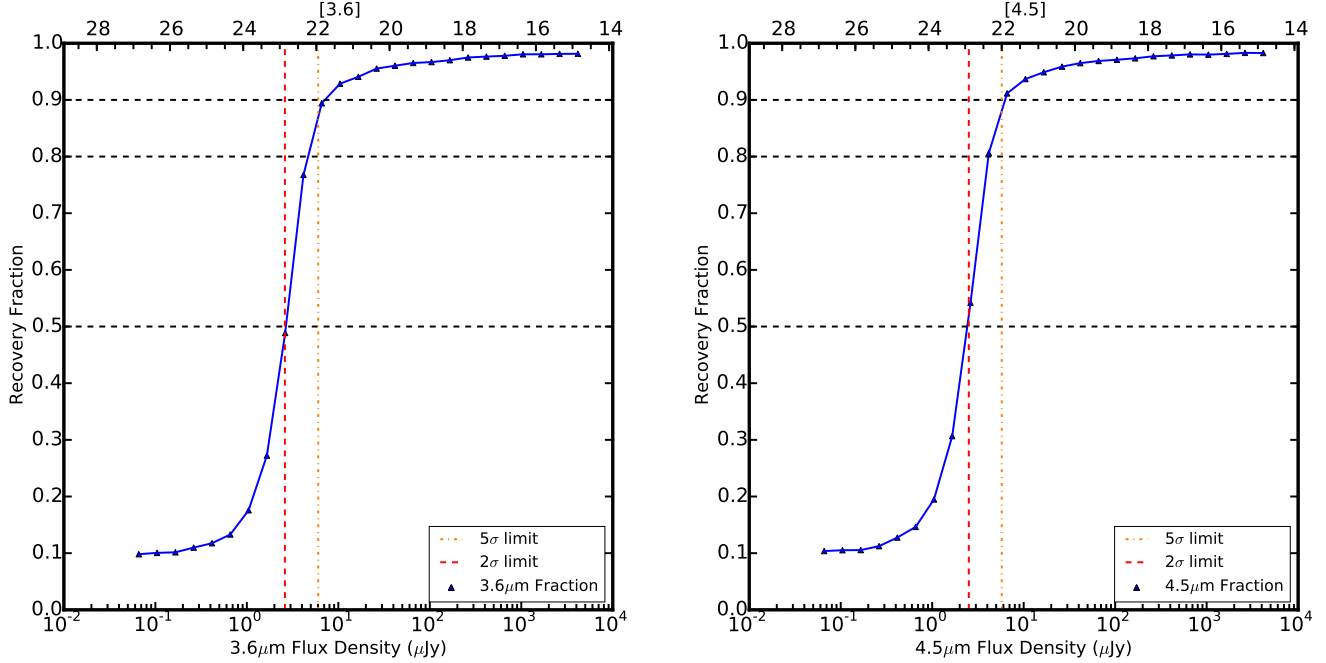
---

[32]http://ssc.spitzer.caltech.edu/warmmission/propkit/pet/senspet/

FIG. 12.— Completeness as a function of $3.6\,\mu$m flux density (and [3.6]; left) and $4.5\,\mu$m flux density (and [4.5]; right) of our simulated sources. The orange dot-dashed line marks the faintest detection of (5σ) objects at $6.13\,\mu$Jy and $5.75\,\mu$Jy at $3.6\,\mu$m and $4.5\,\mu$m, respectively; the red dashed line shows (2σ) objects at 2.58μJy and 2.47μJy at $3.6\,\mu$m and $4.5\,\mu$m, respectively, as measured from the curves in Figure 14. The completeness curves are less affected by artifacts at faint magnitudes since the analysis is done with simulated sources, and thus are better estimates of depth than the number counts.
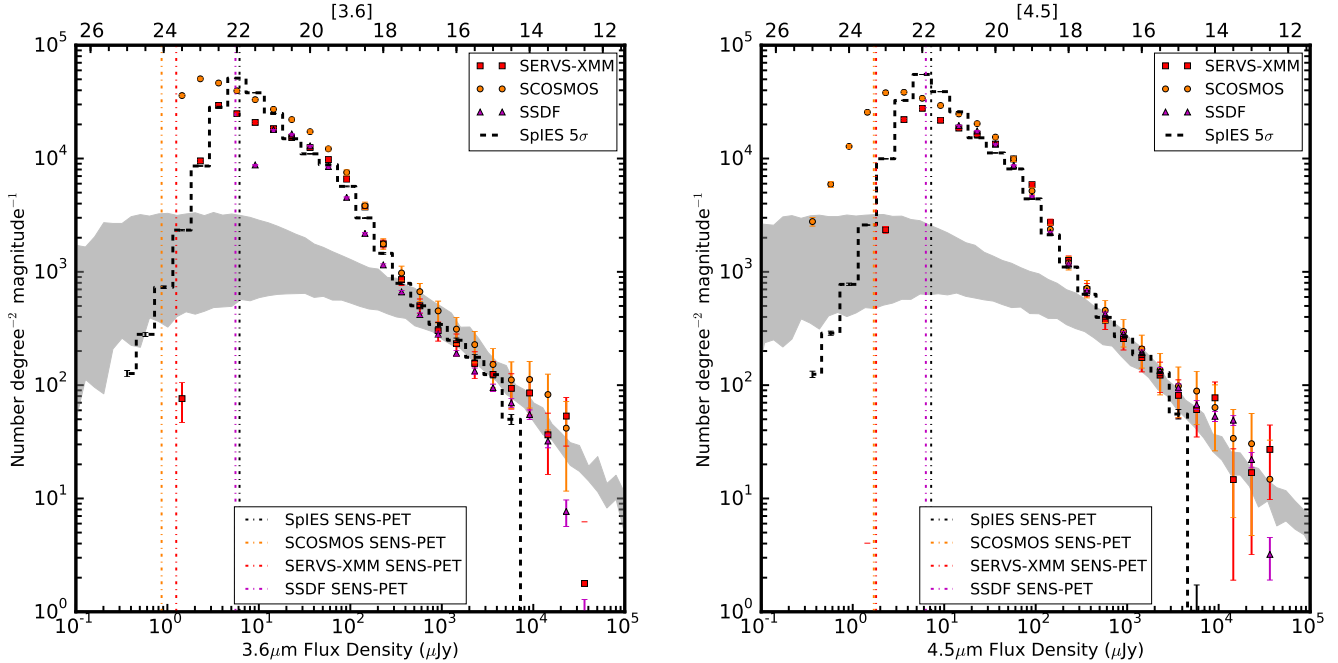

FIG. 13.— Differential number counts per magnitude over the full SpIES field for all objects with a HIGH_REL > 0. In both panels, we divide the counts by an area of 101 deg^2 which is the area covered for this footprint in each detector. Left: SpIES 5σ catalog (black dash) histogram of number of objects per square degree vs flux density (μJy) for all objects detected at $3.6\,\mu$m. Also shown are the number counts from the SERVS XMM field (Mauduit et al. 2012; red squares), S-COSMOS (Sanders et al. 2007; orange circles), and SSDF (Ashby et al. 2013; purple triangles) as comparisons. The dot-dashed lines represent the predicted depth for each survey (see Section 5.5 for more details). As we include objects that are more than 5σ above the background, but have S/N < 5, the excess relative to other surveys near the 90% completeness limit is likely an indication of contamination by low probability sources. Right: The $4.5\,\mu$m number counts similar to the left panel. The grey shaded region shows the contribution of Milky Way stars using the DIRBE Faint Source Model (Arendt et al. 1998; Wainscoat et al. 1992).
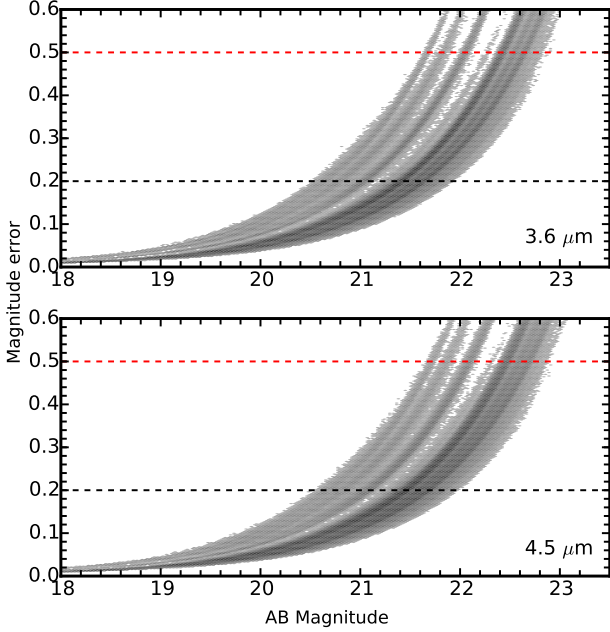
FIG. 14.— Estimation of the the SpIES detection limit at $3.6\,\mu$m (top) and $4.5\,\mu$m (bottom). The grey points indicate the error in magnitude vs. magnitude. The 5σ limit occurs at a magnitude error of 0.2 (black dashed line), and the 2σ limit occurs at a magnitude error of 0.5 (red dashed line). These values are determined by propagating the error in the expression for magnitude, resulting in the ratio of noise to signal as the error in magnitude. The intersection of the right edge of the grey points with the respective magnitude error is the approximate detection threshold. Differences in shading indicates the density of points.

TABLE 9
COMPLETENESS LEVELS

Level	$3.6\,\mu$m		$4.5\,\mu$m	
90% complete	21.75	7.2μJy	21.90	6.3μJy
80% complete	22.20	4.8μJy	22.37	4.1μJy
50% complete	22.82	2.7μJy	22.91	2.5μJy
5σ	21.93	6.13μJy	22.00	5.75μJy
2σ	22.87	2.58μJy	22.92	2.47μJy
$5\sigma_{bg}$	21.62	8.14μJy	21.70	7.55μJy
$2\sigma_{bg}$	22.62	3.26μJy	22.70	3.02μJy
SENS-PET 5σ	21.93	6.15μJy	21.76	7.20μJy

NOTE. — We give the 90, 80 and 50 percent completeness levels in AB Magnitudes and flux density of the SpIES survey from Figure 12 as well as the 5σ and 2σ values from Figure 14, the empty aperture measurements at $5\sigma_{bg}$ and $2\sigma_{bg}$, and the SENS-PET estimates.

5.7. *Confusion*

We estimate the threshold for source confusion (the noise attributed to faint or unresolved background sources) by calculating the average number of SpIES beams per source, similar to the technique used in Ashby et al. (2009), and compare with the classical threshold limits determined in Condon (1974) and Hogg (2001). The SpIES beam size (solid angle) is calculated using $\Omega = \pi\sigma^2$, where σ is the standard deviation of the Gaussian point spread function. Using the relation FWHM $= 2\sqrt{2\ln(2)}\sigma$ and the "warm" IRAC FWHM values of $1\farcs95$ in the $3.6\,\mu$m detector and $2\farcs02$ in the

$4.5\,\mu$m detector, we obtain a beam size of 2.155 arcsec² for the $3.6\,\mu$m detector and 2.312 arcsec² for the $4.5\,\mu$m detector. The total number of beams over the full SpIES area is 6.92×10^8 in the $3.6\,\mu$m images and 6.45×10^8 in the $4.5\,\mu$m images. Finally, taking the ratio of the number of beams to the number of objects at different detection thresholds yields an estimate for the confusion.

There are a total of $\sim 11.6\times 10^6$ objects detected at $3.6\,\mu$m (combining the $3.6\,\mu$m-only catalog and the dual-band catalog) and $\sim 12.1\times 10^6$ objects detected at $4.5\,\mu$m (combining the $4.5\,\mu$m-only catalog and the dual-band catalog) before applying flags for known contaminants, thus there are ~ 60 beams per source and ~ 53 beams per source for the full $3.6\,\mu$m and $4.5\,\mu$m detection catalogs, respectively. Taking the inverse of these two results suggest that approximately 1.6% of the detections at $3.6\,\mu$m and 1.9% of the detections at $4.5\,\mu$m are confused. Condon (1974) and Hogg (2001) found the threshold for confusion to be significant when there are fewer than 30 to 50 beams per source for number counts histograms which have power law slopes of 0.75 to 1.5. The SpIES number counts histograms have slopes of ~ 0.85 for both bands, therefore, with 60 and 53 beams per source at $3.6\,\mu$m and $4.5\,\mu$m, respectively, we conclude that SpIES is not significantly affected by source confusion.

6. DIAGNOSTICS AND SUMMARY

6.1. *Color Distributions*

To test the accuracy of our data processing, we examine the distribution of magnitudes and colors of SpIES sources and compare them to known objects and infrared photometry from *WISE*. Mid-infrared color-color diagrams have proven to be effective in classifying objects, for example quasars, as shown in Lacy et al. (2004), Stern et al. (2005), and Donley et al. (2012). Unlike these previous IRAC analyses, which had access to all four channels, SpIES only observes in the first two, thus instead of a color-color diagram, we investigate the color-magnitude space shown in Figure 15. All SpIES sources with HIGH_REL=2 (in both bands) from the dual-band catalog are shown, along with stars and spectroscopically-confirmed quasars at different redshifts which are detected in the optical and in *WISE* from the Richards et al. (2015) "master" quasar catalog. The "master" catalog is a combination of spectroscopically-confirmed quasars from SDSS-I/II/III (York et al. 2000; Eisenstein et al. 2011) matched with photometric sources from the AllWISE survey. The *WISE* Vega magnitudes have been converted to AB magnitudes by adding 2.699 to W_1 and 3.339 to W_2 which is the difference in the respective zero points for the *WISE* detectors. The *WISE* AB magnitudes were then converted to the *Spitzer* AB system used herein using the color corrections of $[3.6]=W_1(AB)-0.028$ and $[4.5]=W_2(AB)+0.013$ assuming a power-law spectral energy distribution (see Section 2.3 of Richards et al. 2015 and Table 1 of Wright et al. 2010 for more details). We have also included new $z>5$ quasars from McGreer et al. (2013) and the SDSS DR12 quasar catalog (Pâris et al. 2016, in preparation) to this catalog. Figure 15 demonstrates that SpIES can be used to distinguish various types of objects in the mid-infrared. Stars, for example, appear redder than low-redshift ($z \leq 2.2$) quasars, which tend to lie in a
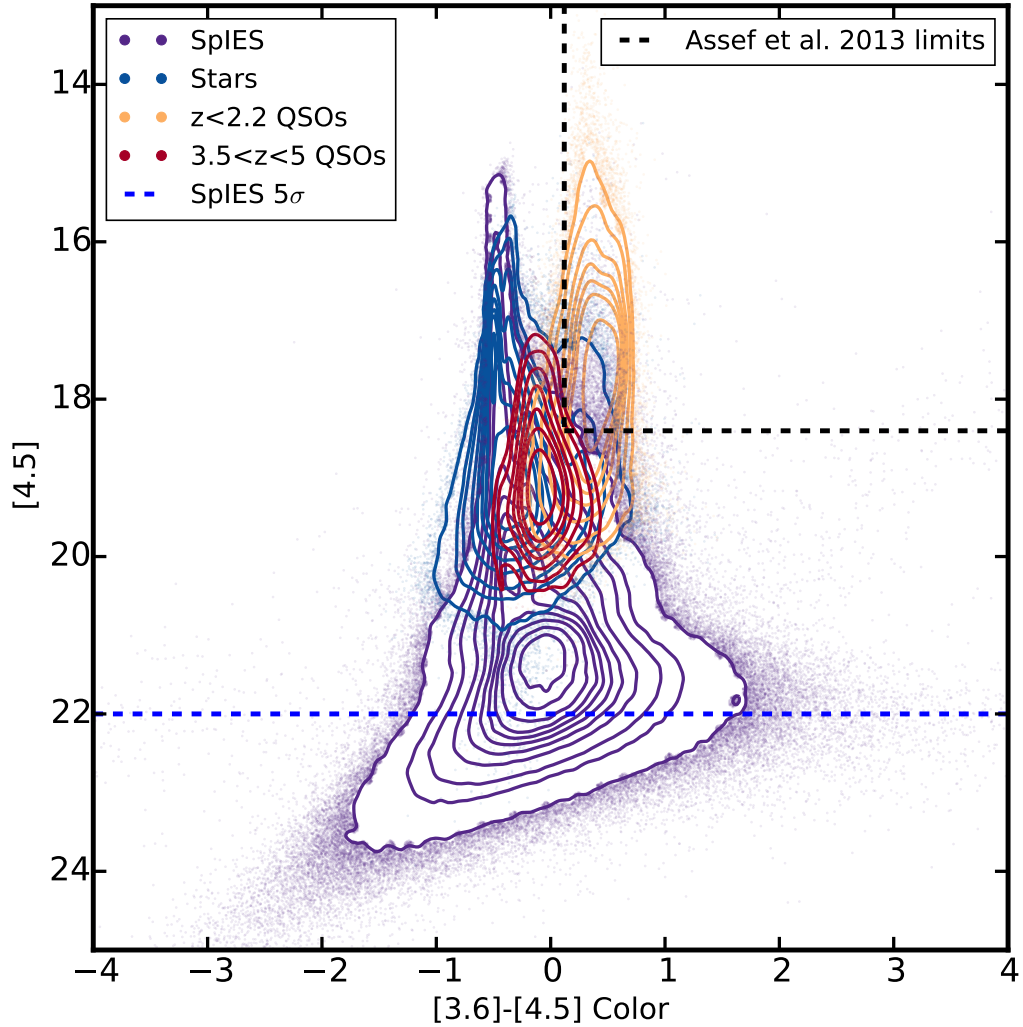
FIG. 15.— Color-magnitude diagram for all detected SpIES objects (purple). Also indicated are contours of where different objects fall in this color space. The blue contours are stars, light orange contours are known low-redshift quasars ($z \leq 2.2$), and red contours are high-redshift quasars ($3.5 \leq z \leq 5$). These additional contours are not objects matched to SpIES data, rather are SDSS detections which have *Spitzer* color information. We show the superior depth of the SpIES survey (the blue dashed line is the [4.5]=22.00 5σ line) compared to the star and quasar data from the optical. The black dashed lines represent the Assef et al. (2013) criteria for AGN selection in this color space ($W1$-$W2 \geq 0.8$), which, although very complete for low-redshift quasars (obscured and unobscured), misses most high-redshift quasars (e.g., Richards et al. 2015).

bluer region of this diagram, despite covering approximately the same magnitude range at $4.5\,\mu$m. It is also apparent that SpIES is achieving a depth that exceeds that of the spectroscopic quasar sample shown.

6.2. *SDSS quasars*

Figure 16 displays $[3.6]-$W1 vs $[4.5]-$W2 for the confirmed quasars in the Richards et al. (2015) "master" quasar catalog. In theory, we might expect the quasar colors to converge at the origin, however there is a deviation of the colors from the origin which can be attributed to a few factors. First, SpIES and the AllWISE surveys were conducted at different times, and thus variable quasars would shift diagonally in this color space. Additionally, there is a well-known flux underestimation bias for fainter objects in the AllWISE data attributed to an overestimation of the background caused by contamination of nearby objects, forcing the *WISE* colors to appear fainter (see the AllWISE Explanatory Supplement[33] for more detail).

One of the goals of SpIES is to uncover new, faint quasars at high-redshift to use for clustering investigations. Discovery of such objects is beyond the scope of this paper, but we show here that the SpIES data are capable of recovering such objects and have a greater ability to do so than can be achieved with the shallower *WISE* data. Figure 17 shows redshift and i-band magnitude histograms of sources using the "master" quasar catalog from Richards et al. (2015) as before. *WISE* only recovers 55% of the quasars in this sample, while SpIES has superior resolution and is sufficiently deep to recover 98%, including objects as faint as 22nd magnitude (i-band) and redshifts as high as 6. As one of the key science goals of the SpIES program is the discovery of faint, high-redshift quasars, we note that SpIES recovers 94% of these quasars with $z \geq 3.5$ as opposed to the 25% recovered by the *WISE* data, and 3.5% recovered after applying the Assef et al. (2013) color cuts.

6.3. *Summary*

The *Spitzer* IRAC Equatorial Survey is supplying large-area, mid-infrared imaging of the Sloan Digital Sky Survey field Stripe 82. Utilizing mapping mode with 'warm' IRAC, SpIES covers a total of $\sim$115 deg^2 of S82 (where there is $\sim$100 deg^2 of coverage in both bands) over two epochs, and overlaps with a wealth of ancillary data at almost every wavelength (see Figure 1). We present the initial source catalogs for SpIES. First, a dual-band catalog containing detections in both $3.6\,\mu$m and $4.5\,\mu$m. Second, a $3.6\,\mu$m-only detected catalog and, third, a $4.5\,\mu$m-only detected catalog. In these catalogs, we report positional and photometric information, photometric errors (see Section 5.2), and a number of flags which are used to distinguish the high-reliability sources. The structure and analysis of these catalogs are as follows:

- We detect $\sim$11.6 million in $3.6\,\mu$m and $\sim$12.1 million in $4.5\,\mu$m, of which $\sim$5.4 million are matched between the two bands and are presented in the dual-band catalog. The remaining $\sim$6.1 million

[33]http://wise2.ipac.caltech.edu/docs/release/allsky /expsup/sec6_3c.html#flux_under
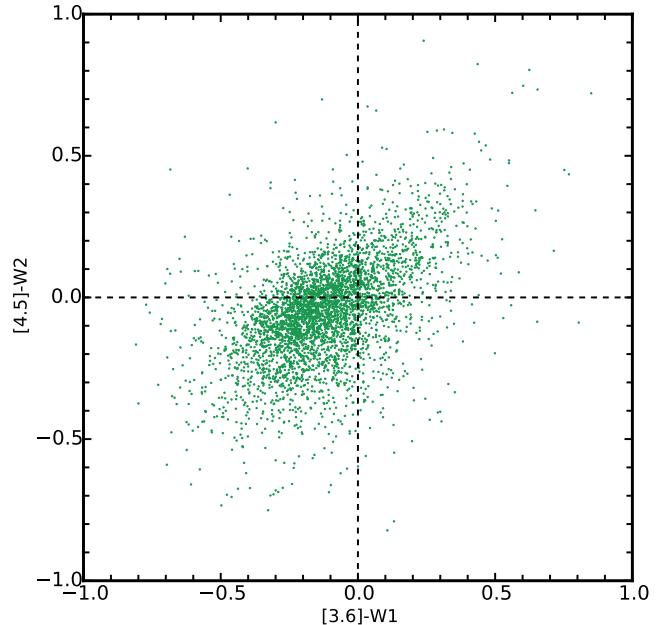

FIG. 16.— Comparison of the SpIES and WISE colors for quasars from the Richards et al. (2015) "master" catalog. WISE Magnitudes have been corrected to the IRAC AB Magnitude system in both channels. In principle, we expect the points to be near the origin, however phenomena such as variability and systematics such as contamination in *WISE* W1 and W2 cause the points to deviate.

in $3.6\,\mu$m and $\sim$6.6 million in $4.5\,\mu$m sources that do not match are retained in the respective single-band only catalogs. $\sim$1.4, $\sim$3.9, and $\sim$1.4 million of these sources ($3.6\,\mu$m-only, dual-band, 4.5μm-only) are considered reliable sources (i.e, HIGH_REL>0 and S/N>3). Much of our data analysis was performed on the dual-band catalog since it contains the most reliable sources in the survey.

- Using the objects in the dual-band catalog, we measured the positional accuracy (Figure 11) of the SpIES detections against point sources from SDSS, and have corrected the positions in the three catalogs for the measured offset. The standard deviation of this distribution is $0''\!.0008$ in RA and $0''\!.0006$ in DEC.

- A Monte Carlo estimate of the completeness is given in Figure 12, which shows that SpIES is 90% complete at AB magnitudes of 21.75 (7.2 μJy) and 21.90 (6.3 μJy) at $3.6\,\mu$m and $4.5\,\mu$m, respectively. Additionally, the SpIES number counts are compared with those from previous *Spitzer* surveys (Figure 13) which, along with completeness, can be used as a measure of the survey depth.

- An extensive discussion of the depth is given in Section 5.6 where we compare some of the different methods typically used to measure depth. We show that SpIES has a calculated 5σ depth of $\sim$6.15 μJy and $\sim$7.2 μJy and an empirical 5σ depth from Figure 14 of $\sim$6.13 μJy and $\sim$5.75 μJy at $3.6\,\mu$m and $4.5\,\mu$m respectively. We report the completeness
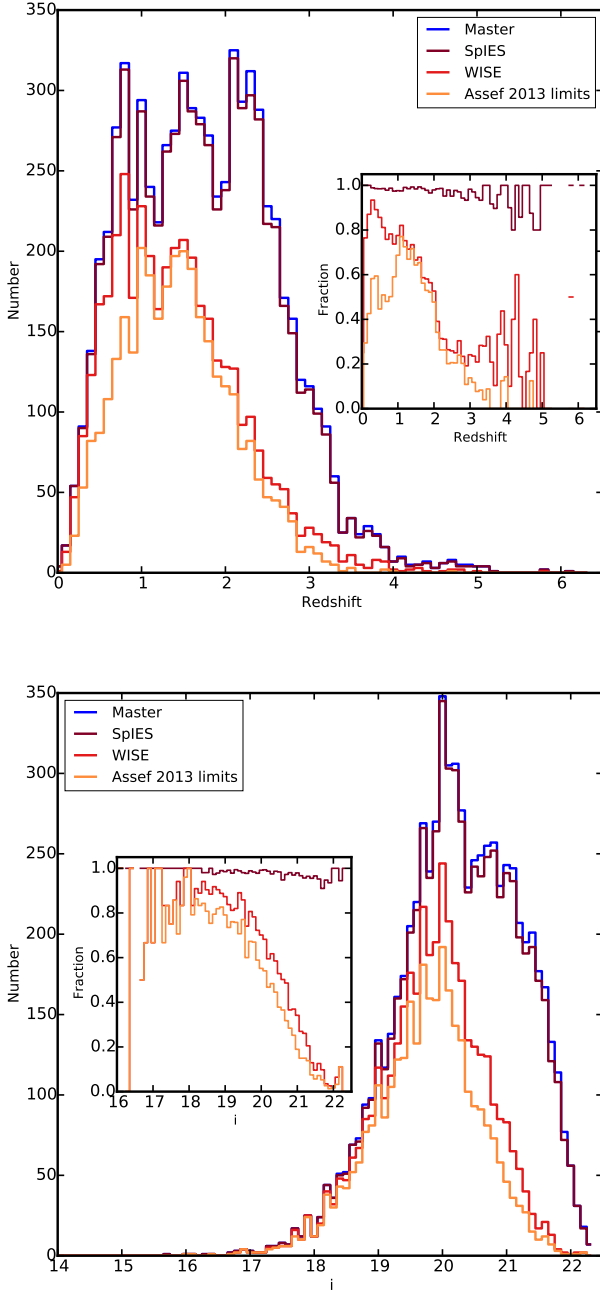
FIG. 17.— Top: Number counts of confirmed quasar redshifts from the optical samples (blue line) in the Richards et al. (2015) "master" catalog, the high-redshift quasars catalog of McGreer et al. (2013), and the SDSS DR12 quasar catalog (Pâris et al. 2016, in preparation). We overplot the redshift distribution of the matched SpIES objects (dark red) and the WISE objects (red) along with the WISE data after applying the Assef et al. (2013) constraints (orange). The number counts have been enhanced by a factor of 5 at $z \geq 3.5$ to emphasize the detections at high redshift. Bottom: The same sample of quasars, using the i-band magnitude as a depth comparison. The inset on both panels is the fraction of objects recovered for SpIES (dark red), WISE (red), and the Assef et al. (2013) objects (orange) with respect to the optical sample.

and depth measurements in Table 9.

- One of the mission goals of SpIES was to be deep enough to detect high-redshift quasars. To test how well SpIES detects these objects, we first examined the colors of different objects in the mid-infrared in Figure 15, and show that SpIES has the capability to detect these high-redshift quasars from the overlap of their mid-infrared colors. From this plot we also see that SpIES detects objects much fainter than the majority of spectroscopically confirmed high-redshift quasars. Finally, the SpIES data were matched to the known quasars in the Richards et al. (2015) "master" quasar catalog and we show that SpIES detects a high percentage of quasars compared to *WISE*, particularly at $z \geq 3.5$ (Figure 17).

The raw imaging data is available on the SHA website, and we now release the mosaics created by the SpIES team and our three detection catalogs for public use (see Appendix A).

Facility:*Spitzer* (IRAC)

APPENDIX

HOW TO ACCESS THE RAW DATA, IMAGE AND CATALOGS

Raw Data

The raw data for SpIES can be found on the *Spitzer* Heritage Archive website `http://sha.ipac.caltech.edu/`, where the user can input the SpIES program number (90045) and select the data type (BCD image, pBCD image, AOR).

Catalogs and Images

The three detection catalogs and all of the images created by the SpIES team can be found at `http://www.physics.drexel.edu/~gtr/spies/`. These files have been compressed for convenience.

APPENDIX

THE SPIES ASTRONOMICAL OBSERVATION REQUESTS

TABLE 10
Full SpIES AOR list

Number	SpIES AOR Label (IRACPC-SPIES-)	AOR Key	RA (J2000) (degrees)	DEC (J2000) (degrees)	Obs. Start	Obs. End	Integration time (s)
1	22634	46949888	331.760	0.008333	2013-01-15 12:22:18	2013-01-15 15:36:43	11945
2	22647	46945024	331.812	−0.008333	2013-01-14 20:03:50	2013-01-14 23:18:21	11956
3	22915	46973952	332.275	0.008333	2014-09-06 22:29:12	2014-09-07 04:59:07	23788
4	22927	46970880	332.327	−0.008333	2014-09-06 11:07:02	2014-09-06 17:36:43	23772
5	221156	46943744	332.984	0.008333	2014-09-07 10:38:37	2014-09-07 15:50:27	19075
6	22128.	46955520	333.036	−0.008333	2014-09-07 05:25:54	2014-09-07 10:37:40	19069
7	221436	46969856	333.654	0.008333	2014-09-07 21:12:36	2014-09-08 02:24:23	19072
8	221449	46966784	333.706	−0.008333	2014-09-07 16:00:01	2014-09-07 21:11:40	19064
9	221717	46955264	334.324	0.008333	2014-09-08 16:45:17	2014-09-08 21:57:09	19075
10	221730	46950144	334.376	−0.008333	2014-09-08 03:03:36	2014-09-08 08:15:14	19061
11	221958	46980864	335.032	0.008333	2014-09-13 16:18:01	2014-09-13 22:10:02	21503
12	222011	46947584	335.084	−0.008333	2014-09-13 10:24:42	2014-09-13 16:16:39	21500
13	222239	46977792	335.664	0.008333	2013-01-15 17:50:48	2013-01-15 23:03:16	19071
14	222251	46972416	335.716	−0.008333	2013-01-15 06:51:52	2013-01-15 12:04:24	19079
15	222520	46962176	336.334	0.008333	2013-01-15 01:38:25	2013-01-15 06:51:06	19091
16	222532	46958080	336.386	−0.008333	2013-01-14 09:22:06	2013-01-14 14:34:48	19101
17	22280.	46948608	337.004	0.008333	2013-01-14 04:08:28	2013-01-14 09:21:20	19111
18	222813	46943488	337.056	−0.008333	2013-01-13 22:45:08	2013-01-14 03:58:33	19115
19	223041	46945536	337.674	0.008333	2013-01-13 17:30:51	2013-01-13 22:44:22	19127
20	223054	46942208	337.726	−0.008333	2013-01-13 12:16:22	2013-01-13 17:29:57	19131
21	223322	46971392	338.344	0.008333	2013-01-13 06:52:39	2013-01-13 12:06:22	19143
22	223335	46968064	338.396	−0.008333	2013-01-13 01:37:58	2013-01-13 06:51:45	19147
23	22363.	46948096	339.014	0.008333	2014-09-14 21:53:31	2014-09-15 04:24:01	23819
24	223615	46953984	339.066	−0.008333	2014-09-14 15:22:11	2014-09-14 21:52:32	23810
25	223844	46942464	339.684	0.008333	2013-01-20 02:13:16	2013-01-20 07:25:31	19065
26	223856	46978816	339.736	−0.008333	2013-01-19 15:34:17	2013-01-19 20:46:34	19072
27	224124	46979584	340.354	0.008333	2014-09-17 15:56:43	2014-09-17 21:48:42	21487
28	224137	46976000	340.406	−0.008333	2014-09-17 10:03:25	2014-09-17 15:55:19	21483
29	22445.	46951680	341.024	0.008333	2013-01-18 22:36:06	2013-01-19 03:49:14	19102
30	224418	46962432	341.076	−0.008333	2013-01-18 17:22:04	2013-01-18 22:35:12	19106
31	224646	46952448	341.694	0.008333	2013-01-20 12:50:36	2013-01-20 18:03:20	19089
32	224659	46949376	341.746	−0.008333	2013-01-20 07:26:56	2013-01-20 12:39:42	19093
33	224927	46976512	342.364	0.008333	2013-01-22 12:04:10	2013-01-22 17:16:26	19068
34	224939	46973184	342.416	−0.008333	2013-01-22 06:42:00	2013-01-22 11:54:18	19072
35	22528.	46951168	343.034	0.008333	2013-01-18 06:42:57	2013-01-18 11:56:32	19139
36	225220	46969600	343.086	−0.008333	2013-01-18 12:07:13	2013-01-18 17:20:49	19136
37	225448	46960896	343.704	0.008333	2013-01-19 04:56:31	2013-01-19 10:09:46	19135
38	22551.	46952192	343.756	−0.008333	2013-01-19 10:10:41	2013-01-19 15:23:53	19132
39	225729	46946560	344.374	0.008333	2013-01-22 01:28:02	2013-01-22 06:40:47	19104
40	225742	46980352	344.426	−0.008333	2013-01-21 13:15:52	2013-01-21 18:28:43	19111
41	23010	46967040	345.044	0.008333	2014-09-22 01:15:20	2014-09-22 07:07:07	21486
42	23023	46963712	345.096	−0.008333	2014-09-22 07:08:28	2014-09-22 13:00:19	21489
43	23251	46953472	345.714	0.008333	2013-01-20 18:05:04	2013-01-20 23:18:42	19140
44	2333.	46978304	345.766	−0.008333	2013-01-20 23:35:28	2013-01-21 04:49:06	19138
45	23532	46977280	346.345	0.008333	2014-09-19 05:22:35	2014-09-19 11:13:11	21404
46	23544	46974464	346.397	−0.008333	2014-09-19 11:14:33	2014-09-19 17:05:15	21409
47	23812	46963968	347.054	0.008333	2014-09-20 05:39:13	2014-09-20 10:50:41	19061
48	23825	46959360	347.106	−0.008333	2014-09-20 10:51:35	2014-09-20 16:03:08	19064
49	231053	46954752	347.724	0.008333	2014-09-21 10:03:17	2014-09-21 15:15:05	19075
50	23116.	46971136	347.776	−0.008333	2014-09-21 15:15:59	2014-09-21 20:27:49	19076
51	231334	46978560	348.394	0.008333	2014-09-24 03:00:32	2014-09-24 08:13:02	19104
52	231347	46975232	348.446	−0.008333	2014-09-23 21:47:10	2014-09-24 02:59:36	19101
53	231615	46964480	349.064	0.008333	2014-09-24 08:23:13	2014-09-24 13:35:39	19097
54	231627	46960640	349.116	−0.008333	2014-09-24 13:36:33	2014-09-24 18:49:04	19101
55	231856	46951936	349.734	0.008333	2014-09-27 06:29:48	2014-09-27 11:42:33	19133
56	23198.	46961664	349.786	−0.008333	2014-09-26 15:23:00	2014-09-26 20:35:32	19124
57	232136	46949120	350.404	0.008333	2013-01-29 18:01:35	2013-01-29 23:13:56	19078
58	232149	46944000	350.456	−0.008333	2013-01-29 12:48:22	2013-01-29 18:00:42	19083
59	232417	46972928	351.074	0.008333	2013-01-27 06:05:06	2013-01-27 11:18:22	19121
60	232430	46968320	351.126	−0.008333	2013-01-27 00:51:00	2013-01-27 06:04:12	19125
61	232658	46959104	351.744	0.008333	2013-01-25 07:06:46	2013-01-25 12:20:32	19159
62	232711	46954240	351.796	−0.008333	2013-01-24 10:56:43	2013-01-24 16:10:41	19172
63	232939	46944512	352.414	0.008333	2013-01-27 16:42:59	2013-01-27 21:56:29	19134
64	232951	46979072	352.466	−0.008333	2013-01-27 11:28:32	2013-01-27 16:42:05	19138
65	233220	46979840	353.084	0.008333	2013-01-25 17:44:54	2013-01-25 22:58:59	19171
66	233232	46976256	353.136	−0.008333	2013-01-25 12:21:49	2013-01-25 17:35:53	19176

TABLE 10 — *Continued*

Number	SpIES AOR Label (IRACPC-SPIES-)	AOR Key	RA (J2000) (degrees)	DEC (J2000) (degrees)	Obs. Start	Obs. End	Integration time (s)
67	23350.	46966272	353.754	0.008333	2013-09-24 20:07:15	2013-09-25 01:20:29	19129
68	233513	46962944	353.806	−0.008333	2013-09-24 14:53:12	2013-09-24 20:06:19	19126
69	233741	46952960	354.424	0.008333	2013-09-27 05:28:49	2013-09-27 10:42:24	19155
70	233754	46949632	354.476	−0.008333	2013-09-26 23:28:02	2013-09-27 04:41:30	19150
71	234022	46950656	355.094	0.008333	2013-09-26 18:13:41	2013-09-26 23:26:56	19138
72	234035	46945792	355.146	−0.008333	2013-09-26 07:33:02	2013-09-26 12:46:05	19131
73	23433.	46965760	355.764	0.008333	2013-09-23 23:03:13	2013-09-24 04:16:06	19092
74	234315	46971648	355.816	−0.008333	2013-09-23 02:21:37	2013-09-23 07:34:09	19076
75	234544	46961152	356.434	0.008333	2013-09-24 09:39:16	2013-09-24 14:51:42	19089
76	234556	46957568	356.486	−0.008333	2013-09-24 04:16:58	2013-09-24 09:29:46	19086
77	234824	46947072	357.104	0.008333	2013-09-27 15:57:49	2013-09-27 21:11:02	19124
78	234837	46943232	357.156	−0.008333	2013-09-27 10:43:48	2013-09-27 15:56:53	19120
79	23515.	46969088	357.774	0.008333	2014-10-01 09:05:27	2014-10-01 14:17:10	19081
80	235118	46980096	357.826	−0.008333	2014-10-01 14:18:04	2014-10-01 19:29:53	19083
81	235346	46970624	358.444	0.008333	2014-10-01 03:44:12	2014-10-01 08:55:37	19062
82	235359	46967808	358.496	−0.008333	2014-09-30 22:32:02	2014-10-01 03:43:17	19052
83	235627	46956288	359.114	0.008333	2014-10-06 05:30:49	2014-10-06 10:43:44	19132
84	235639	46953216	359.166	−0.008333	2014-10-06 00:17:04	2014-10-06 05:29:53	19130
85	23598.	46956800	359.784	0.008333	2014-10-05 18:54:42	2014-10-06 00:07:17	19119
86	235920	46974976	359.836	−0.008333	2014-10-05 08:23:09	2014-10-05 13:35:37	19112
87	0148	46974208	0.454	0.008333	2013-02-01 07:42:52	2013-02-01 12:56:56	19178
88	021.	46964736	0.506	−0.008333	2013-02-01 02:27:55	2013-02-01 07:41:58	19184
89	0429	46958848	1.124	0.008333	2013-09-30 00:07:47	2013-09-30 05:20:39	19103
90	0442	46954496	1.176	−0.008333	2013-09-30 05:21:33	2013-09-30 10:34:33	19106
91	0710	46942720	1.794	0.008333	2013-09-30 16:20:56	2013-09-30 21:33:54	19103
92	0723	46978048	1.846	−0.008333	2013-09-30 21:43:31	2013-10-01 02:56:33	19106
93	0951	46969344	2.464	0.008333	2013-10-01 02:57:20	2013-10-01 08:10:19	19101
94	0103.	46965504	2.516	−0.008333	2013-10-01 19:30:29	2013-10-02 00:43:36	19108
95	01232	46964224	3.134	0.008333	2013-10-02 00:53:18	2013-10-02 06:06:01	19104
96	01244	46960384	3.186	−0.008333	2013-10-02 07:03:50	2013-10-02 12:16:38	19107
97	01512	46950912	3.804	0.008333	2013-10-03 01:26:08	2013-10-03 06:39:09	19108
98	01525	46946304	3.856	−0.008333	2013-10-03 19:40:08	2013-10-04 00:53:17	19119
99	01753	46975488	4.474	0.008333	2013-10-04 22:50:39	2013-10-05 04:03:46	19127
100	0186.	46953728	4.526	−0.008333	2013-10-05 10:58:43	2013-10-05 16:11:57	19132
101	02034	46972672	5.144	0.008333	2013-10-05 16:12:44	2013-10-05 21:25:58	19127
102	02047	46970112	5.196	−0.008333	2013-10-05 21:35:40	2013-10-06 02:49:00	19129
103	02315	46958336	5.814	0.008333	2014-10-08 18:12:29	2014-10-08 23:24:09	19074
104	02327	46955776	5.866	−0.008333	2014-10-08 12:50:34	2014-10-08 18:02:28	19064
105	02556	46944256	6.484	0.008333	2014-10-09 06:57:36	2014-10-09 12:09:18	19072
106	0268.	46956544	6.536	−0.008333	2014-10-09 01:45:09	2014-10-09 06:56:41	19064
107	02836	46970368	7.154	0.008333	2014-10-12 21:56:43	2014-10-13 03:09:07	19118
108	02849	46967552	7.206	−0.008333	2014-10-13 03:19:55	2014-10-13 08:32:24	19120
109	03117	46968576	7.824	0.008333	2014-10-13 08:33:11	2014-10-13 13:45:38	19115
110	03130	46962688	7.876	−0.008333	2014-10-13 13:46:32	2014-10-13 18:59:06	19118
111	03358	46955008	8.494	0.008333	2014-10-15 02:56:10	2014-10-15 08:09:03	19130
112	03411	46948352	8.546	−0.008333	2014-10-14 21:33:39	2014-10-15 02:46:29	19126
113	03639	46979328	9.164	0.008333	2014-10-13 21:13:54	2014-10-14 02:26:13	19102
114	03651	46973440	9.216	−0.008333	2014-10-14 02:27:07	2014-10-14 07:39:31	19103
115	03920	46963200	9.834	0.008333	2014-10-15 08:10:08	2014-10-15 13:22:49	19115
116	03932	46958592	9.886	−0.008333	2014-10-15 19:29:13	2014-10-16 00:42:02	19120
117	0420.	46960128	10.504	0.008333	2014-10-16 06:05:16	2014-10-16 11:17:42	19119
118	04213	46957056	10.556	−0.008333	2014-10-16 00:42:52	2014-10-16 05:55:36	19115
119	04441	46946816	11.174	0.008333	2014-10-16 17:26:02	2014-10-16 22:38:30	19117
120	04454	46942976	11.226	−0.008333	2014-10-16 22:39:24	2014-10-17 03:51:59	19119
121	04722	46971904	11.844	0.008333	2014-10-18 16:32:54	2014-10-18 21:45:50	19133
122	04735	46968832	11.896	−0.008333	2014-10-18 05:01:26	2014-10-18 10:14:13	19126
123	0503.	46959872	12.514	0.008333	2014-10-19 03:09:25	2014-10-19 08:22:23	19130
124	05015	46966016	12.566	−0.008333	2014-10-18 21:46:41	2014-10-19 02:59:33	19127
125	05244	46956032	13.184	0.008333	2014-10-17 23:34:29	2014-10-18 04:46:50	19103
126	05256	46952704	13.236	−0.008333	2014-10-17 18:21:21	2014-10-17 23:33:34	19098
127	05524	46980608	13.854	0.008333	2014-10-20 21:34:09	2014-10-21 02:47:05	19136
128	05537	46976768	13.906	−0.008333	2014-10-20 16:20:23	2014-10-20 21:33:14	19133
129	1490	46967296	27.254	0.008333	2013-10-18 17:40:42	2013-10-18 22:51:25	18965
130	14913	46963456	27.306	−0.008333	2013-10-18 22:52:20	2013-10-19 04:03:05	18970
131	15141	46965248	27.924	0.008333	2013-10-19 11:07:27	2013-10-19 16:18:12	18968
132	15154	46961408	27.976	−0.008333	2013-10-19 16:19:07	2013-10-19 21:29:53	18970
133	15422	46951424	28.594	0.008333	2013-10-20 13:16:13	2013-10-20 18:27:12	18975
134	15435	46947328	28.646	−0.008333	2013-10-20 18:37:01	2013-10-20 23:47:36	18977
135	1573.	46966528	29.264	0.008333	2013-10-20 23:48:22	2013-10-21 04:58:50	18970
136	15715	46972160	29.316	−0.008333	2013-10-21 10:44:00	2013-10-21 15:54:36	18977
137	15944	46961920	29.934	0.008333	2013-10-21 15:55:22	2013-10-21 21:05:52	18970
138	15956	46957824	29.986	−0.008333	2013-10-21 21:06:45	2013-10-22 02:17:18	18971
139	2224	46977536	30.604	0.008333	2013-10-24 13:46:24	2013-10-24 18:57:49	19021
140	2237	46974720	30.656	−0.008333	2013-10-24 18:58:43	2013-10-25 00:10:09	19022
141	255.	46948864	31.274	0.008333	2013-10-25 00:20:14	2013-10-25 05:31:32	19014
142	2518	46959616	31.326	−0.008333	2013-10-25 08:39:48	2013-10-25 13:51:12	19021

TABLE 10 — *Continued*

Number	SpIES AOR Label (IRACPC-SPIES-)	AOR Key	RA (J2000) (degrees)	DEC (J2000) (degrees)	Obs. Start	Obs. End	Integration time (s)
143	2746	46950400	31.944	0.008333	2013-10-27 01:14:33	2013-10-27 06:26:30	19045
144	2759	46946048	31.996	−0.008333	2013-10-27 11:23:55	2013-10-27 16:35:58	19052
145	21027	46944768	32.614	0.008333	2013-10-28 18:25:44	2013-10-28 23:37:49	19059
146	21039	46981120	32.666	−0.008333	2013-10-28 23:38:43	2013-10-29 04:50:49	19061
147	2138.	46945280	33.284	0.008333	2013-10-31 13:24:25	2013-10-31 18:37:17	19090
148	21320	46964992	33.336	−0.008333	2013-10-31 18:47:26	2013-11-01 00:00:17	19093
149	21548	46957312	33.954	0.008333	2013-11-01 18:29:22	2013-11-01 23:42:19	19098
150	2161.	46947840	34.006	−0.008333	2013-11-01 23:43:13	2013-11-02 04:56:10	19100
151	21829	46941952	34.624	0.008333	2014-11-08 22:10:40	2014-11-09 03:23:03	18801
152	21842	46975744	34.676	−0.008333	2014-11-08 16:48:59	2014-11-08 22:01:17	18801
153	22110	46977024	35.294	0.008333	2014-11-08 11:35:49	2014-11-08 16:47:54	18802
154	22123	46973696	35.346	−0.008333	2014-11-08 06:14:41	2014-11-08 11:26:35	18801

NOTE. — This table shows the single epoch AORs in the SpIES survey. Each set of 2 AORs overlap approximately the same area, for instance, AOR number 1 and 2 overlap with each other to image one region on the sky.

REFERENCES

Alexandroff, R., Strauss, M. A., Greene, J. E., et al. 2013, MNRAS, 435, 3306
Annis, J., Soares-Santos, M., Strauss, M. A., et al. 2014, ApJ, 794, 120
Arendt, R. G., Odegard, N., Weiland, J. L., et al. 1998, ApJ, 508, 74
Ashby, M. L. N., Stern, D., Brodwin, M., et al. 2009, ApJ, 701, 428
Ashby, M. L. N., Stanford, S. A., Brodwin, M., et al. 2013, ApJS, 209, 22
Assef, R. J., Stern, D., Kochanek, C. S., et al. 2013, ApJ, 772, 26
Assef, R. J., Eisenhardt, P. R. M., Stern, D., et al. 2015, ApJ, 804, 27
Astropy Collaboration, Robitaille, T. P., Tollerud, E. J., et al. 2013, Astron. & Astrophys., 558, A33
Becker, R. H., White, R. L., & Helfand, D. J. 1995, ApJ, 450, 559
Bertin, E., & Arnouts, S. 1996, A&AS, 117, 393
Bundy, K., Leauthaud, A., Saito, S., et al. 2015, ArXiv e-prints, arXiv:1509.01276
Coil, A. L., Blanton, M. R., Burles, S. M., et al. 2011, ApJ, 741, 8
Condon, J. J. 1974, ApJ, 188, 279
Croom, S. M., Smith, R. J., Boyle, B. J., et al. 2004, MNRAS, 349, 1397
Croom, S. M., Richards, G. T., Shanks, T., et al. 2009, MNRAS, 392, 19
Daddi, E., Alexander, D. M., Dickinson, M., et al. 2007, ApJ, 670, 173
Das, S., Louis, T., Nolta, M. R., et al. 2014, Journal of Cosmology and Astroparticle Physics, 2014, 014
Davis, M., Guhathakurta, P., Konidaris, N. P., et al. 2007, ApJ Lett., 660, L1
de la Torre, S., Guzzo, L., Peacock, J. A., et al. 2013, Astron. & Astrophys., 557, A54
Diehl, H. T., Abbott, T. M. C., Annis, J., et al. 2014, in Society of Photo-Optical Instrumentation Engineers (SPIE) Conference Series, Vol. 9149, Society of Photo-Optical Instrumentation Engineers (SPIE) Conference Series, 0
Donley, J. L., Koekemoer, A. M., Brusa, M., et al. 2012, ApJ, 748, 142
Drinkwater, M. J., Jurek, R. J., Blake, C., et al. 2010, MNRAS, 401, 1429
Eisenstein, D. J., Weinberg, D. H., Agol, E., et al. 2011, AJ, 142, 72
Fazio, G. G., Hora, J. L., Allen, L. E., et al. 2004, ApJS, 154, 10
Fox, O. D., Johansson, J., Kasliwal, M., et al. 2015, ArXiv e-prints, arXiv:1510.08070 [astro-ph.HE]
Frieman, J. A., Bassett, B., Becker, A., et al. 2008, AJ, 135, 338
Fukugita, M., Ichikawa, T., Gunn, J. E., et al. 1996, AJ, 111, 1748
Glikman, E., Urrutia, T., Lacy, M., et al. 2013, ApJ, 778, 127
Gralla, M. B., Crichton, D., Marriage, T. A., et al. 2014, MNRAS, 445, 460
Helfand, D. J., White, R. L., & Becker, R. H. 2015, ApJ, 801, 26
Hodge, J. A., Becker, R. H., White, R. L., Richards, G. T., & Zeimann, G. R. 2011, AJ, 142, 3
Hogg, D. W. 2001, AJ, 121, 1207
Hopkins, P. F., Richards, G. T., & Hernquist, L. 2007, ApJ, 654, 731
Houck, J. R., Roellig, T. L., van Cleve, J., et al. 2004, ApJS, 154, 18
Hunter, J., Firing, E., Caswell, T. A., et al. 2007, Computing In Science & Engineering, 9, 90

Jarvis, M. J., Bhatnagar, S., Bruggen, M., et al. 2014, ArXiv e-prints, arXiv:1401.4018 [astro-ph.CO]
Jiang, L., Fan, X., Bian, F., et al. 2014, ApJS, 213, 12
Krawczyk, C. M., & Peters, C. M. 2014, densityplot: v1.0.0
Labbe, I., Oesch, P. A., Illingworth, G. D., et al. 2015, ArXiv e-prints, arXiv:1507.08313
Lacy, M., Storrie-Lombardi, L. J., Sajina, A., et al. 2004, ApJS, 154, 166
LaMassa, S. M., Urry, C. M., Glikman, E., et al. 2013a, MNRAS, 432, 1351
LaMassa, S. M., Urry, C. M., Cappelluti, N., et al. 2013b, MNRAS, 436, 3581
—. 2015, ArXiv e-prints, arXiv:1510.00852
Lawrence, A., Warren, S. J., Almaini, O., et al. 2007, MNRAS, 379, 1599
Le Fèvre, O., Vettolani, G., Garilli, B., et al. 2005, Astron. & Astrophys., 439, 845
Lonsdale, C. J., Smith, H. E., Rowan-Robinson, M., et al. 2003, PASP, 115, 897
Lucas, P. W., Tinney, C. G., Burningham, B., et al. 2010, MNRAS, 408, L56
Martin, D. C., Fanson, J., Schiminovich, D., et al. 2005, ApJ Lett., 619, L1
Mauduit, J.-C., Lacy, M., Farrah, D., et al. 2012, PASP, 124, 714
McGreer, I. D., Jiang, L., Fan, X., et al. 2013, ApJ, 768, 105
McMahon, R. G., Banerji, M., Gonzalez, E., et al. 2013, The Messenger, 154, 35
Mooley, K. P., Myers, S. T., Hallinan, G., et al. 2014, in American Astronomical Society Meeting Abstracts, Vol. 223, American Astronomical Society Meeting Abstracts 223, 236.02
Oke, J. B., & Gunn, J. E. 1983, ApJ, 266, 713
Oliver, S. J., Bock, J., Altieri, B., et al. 2012, MNRAS, 424, 1614
Papovich, C., Gebhardt, K., Adams, J., et al. 2011, Spitzer-HETDEX Exploratory Large Area (SHELA) Survey, Spitzer Proposal
Richards, G. T., Myers, A. D., Peters, C. M., et al. 2015, ApJS, 219, 39
Rieke, G. H., Young, E. T., Engelbracht, C. W., et al. 2004, ApJS, 154, 25
Sanders, D. B., Salvato, M., Aussel, H., et al. 2007, ApJS, 172, 86
Schlegel, D. J., Finkbeiner, D. P., & Davis, M. 1998, ApJ, 500, 525
Smee, S. A., Gunn, J. E., Uomoto, A., et al. 2013, AJ, 146, 32
Steinhardt, C. L., Speagle, J. S., Capak, P., et al. 2014, ApJ Lett., 791, L25
Stern, D., Eisenhardt, P., Gorjian, V., et al. 2005, ApJ, 631, 163
Stoughton, C., Lupton, R. H., Bernardi, M., et al. 2002, AJ, 123, 485
Sullivan, M., Conley, A., Howell, D. A., et al. 2010, MNRAS, 406, 782
Surace, J. A., Shupe, D. L., Fang, F., et al. 2005, in Bulletin of the American Astronomical Society, Vol. 37, American Astronomical Society Meeting Abstracts, 1246
Taylor, M. B. 2005, TOPCAT & STIL: Starlink Table/VOTable Processing Software
—. 2006, STILTS - A Package for Command-Line Processing of Tabular Data
Viero, M. P., Asboth, V., Roseboom, I. G., et al. 2014, ApJS, 210, 22
Wainscoat, R. J., Cohen, M., Volk, K., Walker, H. J., & Schwartz, D. E. 1992, ApJS, 83, 111

Wang, W.-H., Cowie, L. L., & Barger, A. J. 2006, ApJ, 647, 74

Werner, M. W., Gallagher, D. B., & Irace, W. R. 2004, Advances in Space Research, 34, 600

White, M., Myers, A. D., Ross, N. P., et al. 2012, MNRAS, 424, 933

Wright, E. L., Eisenhardt, P. R. M., Mainzer, A. K., et al. 2010, AJ, 140, 1868

York, D. G., Adelman, J., Anderson, Jr., J. E., et al. 2000, AJ, 120, 1579